Guar gum solutions for improved delivery of iron particles in porous media (Part 2): Iron transport tests and modeling in radial geometry

Guar gum solutions for improved delivery of iron particles in porous media (Part 2): iron transport tests and modelling in radial geometry

Published in

Journal of Contaminant Hydrology

166 (2014) 34-51

Tiziana Tosco[(1)], Francesca Gastone[(1)], Rajandrea Sethi[(1)]*

[(1)] DIATI – Dipartimento di Ingegneria dell'Ambiente, del Territorio e delle Infrastrutture – Politecnico di Torino, C.so Duca degli Abruzzi 24, 10129 Torino, Italy

* Corresponding Author: phone +39 (011) 564 7735; e-mail: rajandrea.sethi@polito.it

Abstract:

In the present work column transport tests were performed in order to study the mobility of guar-gum suspensions of microscale zero-valent iron particles (MZVI) in porous media. The results were analyzed with the purpose of implementing a radial model for the design of full scale interventions. The transport tests were performed using several concentrations of shear thinning guar gum solutions as stabilizer (1.5, 3 and 4 g/l) and applying different flow rates (Darcy velocity in the range $1 \cdot 10^{-4}$ to $2 \cdot 10^{-3}$ m/s), representative of different distances from the injection point in the radial domain. Empirical relationships, expressing the dependence of the deposition and release parameters on the flow velocity, were derived by inverse fitting of the column transport tests using a modified version of E-MNM1D (Tosco and Sethi, 2010) and the user interface MNMs (www.polito.it/groundwater/software). They were used to develop a comprehensive transport model of MZVI suspensions in radial coordinates, called E-MNM1R, which takes into account the non Newtonian (shear thinning) rheological properties of the dispersant fluid and the porous medium clogging associated with filtration and sedimentation in the porous medium of both MZVI and guar gum residual undissolved particles. The radial model was run in forward mode to simulate the injection of MZVI dispersed in guar gum in conditions similar to those applied in the column transport tests. In a second stage, we demonstrated how the model can be used as a valid tool for the design and the optimization of a full scale intervention. The simulation results indicated that several concurrent aspects are to be taken into account for the design of a successful delivery of MZVI/guar gum slurries via permeation injection, and a compromise is necessary between maximizing the radius of influence of the injection and minimizing the injection pressure, to guarantee a sufficiently

homogeneous distribution of the particles around the injection point and to prevent preferential flow paths.

Keywords:

Microscale iron transport in porous media, guar gum solutions, porous medium flow and transport in radial domains, column transport tests, porous medium clogging.

Graphical abstract:

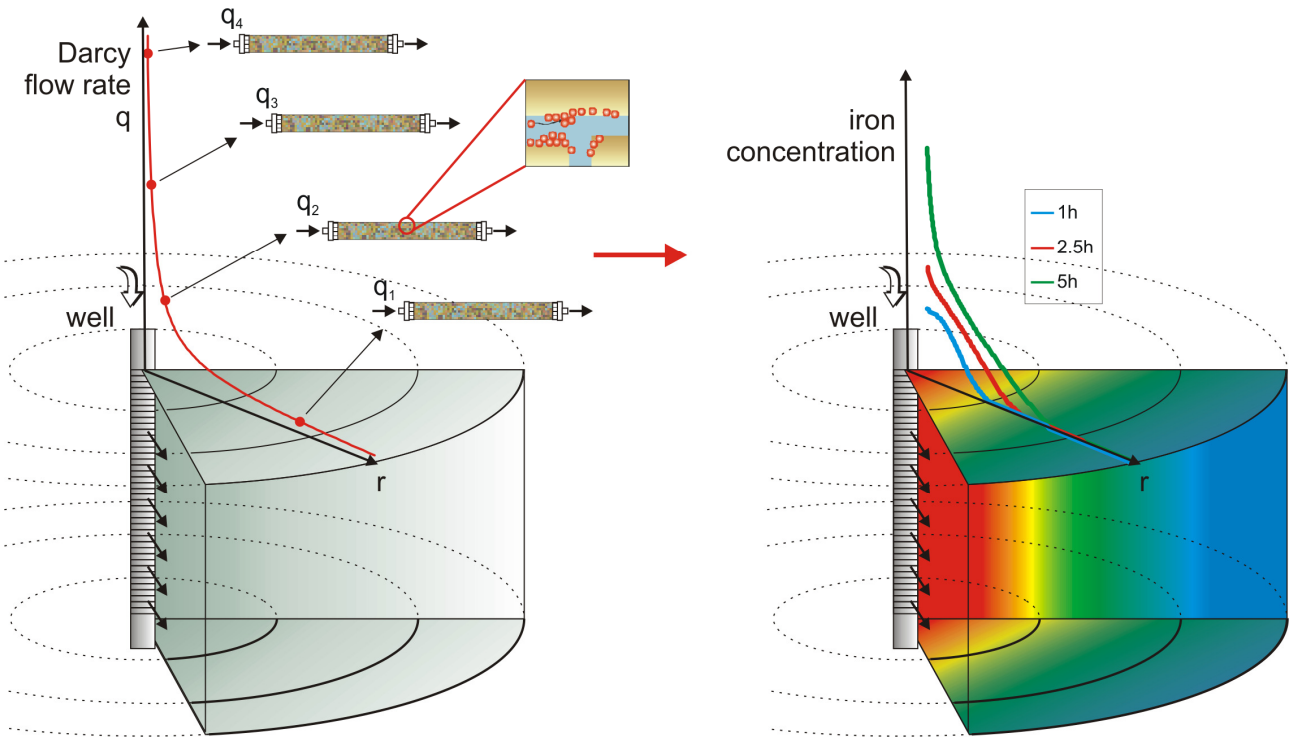

1. Introduction

Nanoscale and microscale iron particles (NZVI and MZVI) show a positive potential for the remediation of contaminated aquifers, in both laboratory and field-scale tests, in particular for the treatment of organic compounds, including widely spread chlorinated hydrocarbons (He and Zhao, 2005; Lien and Zhang, 2001; Liu et al., 2005; Zhang, 2003), pesticides (Elliott et al., 2003; Joo et al., 2004), polycyclic aromatic hydrocarbons (PAHs) (Chang et al., 2005), poly-chloro-biphenyls PCBs (Hadnagy et al., 2004; Lowry and Johnson, 2004), and azo-dyes (Freyria et al., 2011). Compared to other remediation techniques based on the use of millimetric zerovalent iron (namely permeable reactive barriers, PRBs) (Di Molfetta and Sethi, 2006; Zolla et al., 2009), MZVI and NZVI exhibit beneficial peculiarities. In particular, they are characterized by a high specific surface area, orders of magnitude higher than millimetric iron, which results in high degradation rates (Nurmi et al., 2005; Sun et al., 2006). Moreover, they can be injected into the contaminated area dispersed in water-based slurries, thus resulting in a limited occupation of the surface and in a higher flexibility of the technique, compared to other remediation approaches, e.g. permeable reactive barriers (Di Molfetta and Sethi, 2006; Elliott and Zhang, 2003). Finally, it is possible to modify the properties of the particles and of the dispersant fluid, for a tuned delivery and reactivity (Berge and Ramsburg, 2009; Dalla Vecchia et al., 2009b; Quinn et al., 2005; Tiraferri and Sethi, 2009).

Despite the positive characteristics of MZVI and NZVI, some critical aspects are to be addressed before the technology can be applied at the field scale as an established technique. A major issue is associated to the colloidal instability of aqueous dispersions of MZVI and NZVI (Kocur et al., 2013; O'Carroll et al., 2013; Tiraferri and Sethi, 2009; Tosco et al., 2014). Colloidal suspensions of iron particles in the typical concentrations required for field injections (in the order of several grams per liter) are not stable, being NZVI prone to aggregation and consequent sedimentation of the aggregates, and MZVI to sedimentation of the primary particles, with extremely negative impacts on the overall mobility in porous media in both cases (Dalla Vecchia et al., 2009a; Dalla Vecchia et al., 2009b; Saleh et al., 2007; Tiraferri and Sethi, 2009). The lack of stability can be successfully overcome by modifying the surface properties of the particles (approach effective for NZVI) or increasing the viscosity of the dispersant fluid (for MZVI) (Comba et al., 2011; Dalla Vecchia et al., 2009b; Fatisson et al., 2010; Oostrom et al., 2007; Saleh et al., 2007; Tiraferri and Sethi, 2009). In particular, the use of shear thinning solutions of biopolymers was found successful in improving colloidal stability, and consequently mobility, of both MZVI and NZVI in porous media. Among these, visco-elastic fluids (e.g. guar gum - xanthan mixtures) provide an almost indefinitely stable suspension (Xue and Sethi, 2012), while shear thinning solutions without yield stress (e.g. single polymer solutions of guar gum, xanthan, or carboxymethyl cellulose) form suspensions defined as meta-stable, in which the increased viscosity of the polymeric solution reduces the sedimentation rate of the particles (Dalla Vecchia et al., 2009b; Johnson et al., 2013; Kocur et al., 2013; Velimirovic et al., 2012).

The second critical issue to be addressed is related to the mobility of the particles in the porous medium. The suspensions of MZVI and NZVI can be delivered into the subsurface under pressure, resulting in the formation of preferential flow paths and porous medium fracturing (when the

injection pressure overcomes the critical one of the porous medium) or permeation injection, which provides a less heterogeneous distribution of the slurry in the porous medium. The comprehension of the transport mechanisms and the development of a transport model is crucial for field applications. It is necessary to provide an estimation of the expected travel distance and iron distribution, and to identify whether or not the particles will be mobile under the natural flow field. If fracturing delivery is used, the overall distribution of the particles in the subsurface is highly heterogeneous. In this case the estimation of the iron distribution is not based on any transport model, and can be approximated with empirical relationships, since position, extent and width of the fractures in a field application cannot be predicted by numerical modeling (Abdel-Salam and Chrysikopoulos, 1995). Conversely, for permeation injection, modeling approaches based on modified advection-dispersion equations can be adopted (Kocur et al., 2013; Tosco and Sethi, 2010). Great efforts have been devoted so far to the identification of the mechanisms controlling the transport of NZVI (namely physical-chemical interactions with the porous medium, magnetic attraction among particles, filtration and straining of aggregates, sedimentation, etc), and several approaches have been proposed to model its transport and retention in porous media (Kanel et al., 2007; O'Carroll et al., 2013; Petosa et al., 2010; Tiraferri and Sethi, 2009; Torkzaban et al., 2012; Tosco and Sethi, 2010; Yan et al., 2013). On the other hand, fewer studies focused on the mobility of microscale iron (Dalla Vecchia et al., 2009b; Tosco and Sethi, 2010; Velimirovic et al., 2014). In this case, the shear thinning properties of the dispersant fluid, along with the colloidal stability or instability of the suspension, play a major role. The rheological characterization of the MZVI slurries and particles sedimentation was investigated in details by the authors in a previous work (Gastone et al., 2014)

In this work, a study on guar gum-based slurries of MZVI particles is presented. The work is composed by two papers: In Part I, the flow of guar gum solutions in porous media was assessed, evidencing the effects of the shear thinning rheological properties on the pressure build up, and the porous medium clogging caused during injection by residual undissolved particles of guar gum. A model was derived from experimental column filtration tests for the quantification of such processes. In the present Part II, a modeling approach based on the results of laboratory column transport tests is proposed for the simulation of large-scale injection of MZVI via permeation. In field applications fluids are typically injected into the subsurface via wells or direct push systems, generating a radial or radial-like flow, with decreasing velocity with increasing distance from the delivery point (**Figure 1**). Therefore a simplified radial geometry was assumed here. The development of a transport model in radial geometry requires a detailed knowledge of the influence of flow velocity on the kinetics of the particle-porous medium interactions (deposition and release processes), the eventual clogging, and the viscosity of the shear thinning carrier fluid (Ciriello and Di Federico, 2012; Longo et al., 2013; Wexler et al., 2013). However, injection tests at a laboratory scale, which guarantee the well controlled conditions necessary for the development of a mathematical model, are complex and expensive to be realized in a radial flow field. For this reason, in this work the flow velocity dependence of transport processes was investigated in a set of one-dimensional column transport tests, performed at different flow rates, each representative of the flow velocity expected at a different distance from the delivery point. The one-dimensional transport tests were analyzed using a modified formulation of the transport software E-MNM1D (Tosco and Sethi, 2010), the processes governing MZVI transport were identified, and the dependence of the transport parameters on the flow rate and on the fluid viscosity were derived. The obtained relationships were then implemented in the radial model. The radial transport model was

then developed integrating (i) the correlations for the kinetics of MZVI interactions with the porous medium (deposition and release processes) derived from the analysis of column tests, (ii) the results of the companion paper Part I on guar gum flow in porous media (clogging due to undissolved guar gum particles and rheology of guar gum solutions in the porous medium), and (iii) aspects related to the colloidal stability of MZVI slurries dispersed in shear thinning fluids, previously assessed (Gastone et al., 2014). The radial transport model was finally used for direct simulations of MZVI migration in conditions plausible for a full-scale application, varying discharge rate, injected volume, aquifer properties, etc. A methodology for a preliminary dimensioning of a full-scale injection of MZVI slurries is also proposed.

2. Materials and methods

2.1. Materials

Iron particles (HQ from BASF), spherical in shape, with nominal size $d_{10,Fe}$, $d_{50,Fe}$, $d_{90,Fe}$ respectively equal to 0.7, 1.1, 1.8 μm, measured size respectively equal to 0.54, 1.07, 1.53 μm, were purchased and stored as dry powder. The particles are composed by iron (98.4%) and impurities, including carbon (0.69%), nitrogen (0.66%), and oxygen (0.21%). The specific surface of the particles is 705 m^2/kg, the density is $\rho_{Fe} = 7.80 \cdot 10^3$ kg/m^3.

Guar gum provided as dry powder (RANTEC HV7000 from Ranchester, United States) and characterized by a food-grade purity and nominal maximum particle size of 75 μm was used as stabilizer for MZVI dispersions.

High purity sand (Dorsilit # 8 from Dorfner, Germany), composed by quartz (98.9%), with a minor percentage of K-feldspar as microcline (average density of sand: 2.64 g/cm^3) was used in column transport tests. Sand grains are rounded in shape, with nominal size 0.3-0.8 mm, measured size distribution $d_{10,sand}$, $d_{50,sand}$, $d_{90,sand}$ of 0.22, 0.28, 0.33 mm (Static Light Scattering, Beckmann-Coulter LS230, DISAT – Politecnico di Torino), and were pre-treated by the producer by cindering. The cleaning procedures included repeated wet-cleaning (four cycles of rinsing, sonication, and degassing) to remove residual milling dust, impurities, and air bubbles attached to the grain surface.

2.2. Preparation of iron slurries

The guar gum solutions were prepared dissolving the guar gum powder in warm deionized water (60°C). Immediately after preparation, air bubbles were removed degassing the solutions for 5 mins using a vacuum pump. The solutions were stored at 4°C for overnight hydration, and later centrifuged prior to use, to remove residual large undissolved particles (preparation procedure T60C, see details in Gastone et al. (2014)). Sodium azide was added as a preservative.

The iron slurries were prepared immediately prior to use at a particle concentration of 20 g/l, guar gum concentration of 1.5, 3 and 4 g/l, following the procedure described by Xue and Sethi (2012). The iron particles were dispersed in water, sonicated for 5 minutes in order to break aggregates and remove air bubbles, and mixed with the hydrated guar gum solution using a high speed rotor-stator device (UltraTurrax). The slurry was finally degassed 10 mins to remove residual air bubbles.

2.3. Column transport tests

Column tests were performed using Plexiglas columns with 2.4 cm inner diameter, 4 mm thick walls, screwed caps and Plexiglas filters at both ends, specifically designed for high pressure injection. The columns were wet-packed with the sand to a total length of 0.425 m, resulting in average porosity ε_0 = 0.37, bulk density $\rho_b = 1.66 \cdot 10^3$ kg/m^3, specific surface area of the porous medium $a_0 = 1.42 \cdot 10^4$ m^2/m^3, permeability $K_0 = 1.45 \pm 0.30 \cdot 10^{-10}$ m^2. A 1 cm coarse sand pre-filter (d_{50} = 0.9 mm) was applied at both ends to guarantee the homogenization of the flow.

The dispersivity coefficient α_x is assumed here as a constant parameter throughout the injection test, equal to the average grain size, $d_{50,sand}$, following the approximation proposed by Bear for

laboratory-scale solute transport phenomena (Bear, 1988). Changes in α_x can occur during the test due to modifications of the geometry of pores available for flow (Auset and Keller, 2004; Keller et al., 2004; Leij and Bradford, 2013). However, in this work the approximation of constant dispersivity is adopted since hydrodynamic dispersion is expected not to play a predominant role in MZVI transport compared to retention processes.

Progressive cavity pumps (MD 0005-24, Seepex, Germany) were selected for fluid delivery to ensure a constant, non-pulsating flow rate. Separated pumps were used for water and iron slurry injection to avoid mixing of the fluids (**Figure 2**). The transport tests were performed with the columns positioned horizontally, in order to simulate realistic flow conditions which may be altered using vertical columns, due to the MZVI density higher than water (Chrysikopoulos and Syngouna, 2014). The discharge rate was periodically monitored during the test, and variations were always below 1%.

The tests included the following steps:

- pre-flushing of the column with D.I. water (5 PVs)
- iron slurry injection (20 g/l of MZVI, 1.5 g/l, 3 g/l or 4 g/l of guar gum, D.I. water) (10 PVs)
- post-flushing with D.I. water (15 PVs).

The tests were performed injecting guar gum-based slurries of MZVI (polymer concentration c_{GG} = 1.5 g/l, 3 g/l and 4 g/l) at different flow rates, for a total number of 9 different injection conditions. All tests were run in duplicate (**Table 1**). Darcy velocities of $1.1 \cdot 10^{-4}$, $4.3 \cdot 10^{-4}$, $1.2 \cdot 10^{-3}$, and $1.9 \cdot 10^{-3}$ m/s (named in the following q_1, q_2, q_3, and q_4, respectively) were applied. In the tests performed at 3 and 4 g/l of guar gum, the Darcy velocities q_1, q_2, and q_4, were selected. Conversely, for the tests

performed with 1.5 g/l of guar gum, the Darcy velocities q_2, q_3, and q_4 were applied, since q_1 was too low to allow a significant breakthrough of the iron particles, due to the reduced colloidal stability of the suspension at 1.5 g/l of guar gum.

Inline continuous non-invasive measurements of inlet and outlet iron concentration with a time interval of 1 s, as well as profiles of total iron concentration along the column, were performed using susceptibility sensors (MS2G, MS2C and MS2, Bartington, UK). The inlet and outlet concentration of MZVI was continuously monitored inline, with fixed sensors (single frequency sensors MS2G) positioned coaxially to the tubing immediately prior and after the column (**Figure 2** and **Figure 3**). The concentration profiles were measured at the end of the injection step (before flushing) and at the end of the test (after flushing). In this case, the susceptibility sensor (Core logging sensor MS2C) was positioned coaxially to the column, and moved along it for recording the susceptibility, with a space interval of 2 cm. The measured susceptibility profile was then post-processed applying a de-convolution algorithm: the sensor measurement is affected not only by the iron present in the centre of the sensor, but also by the iron located within a coaxial distance of approximately 2.5 diameters (that is, approximately 6 cm before and after the centre of the sensor), with a sensitivity decreasing with distance. As a consequence, a de-correlation of the profiles is required to avoid overestimation of the iron content (Supporting Information).

The measured susceptibility profiles are proportional to the total mass of iron inside the column (that is, iron retained in the porous matrix, and iron eventually present as dispersed colloid in the pore fluid). Consequently, the iron concentration profiles were reported in terms of total iron concentration $c_{tot,Fe}$, calculated as the mass of iron per unit volume of pore space [M L^{-3}], including MZVI particles both deposited and suspended:

$$c_{tot,Fe} = c_{Fe} + \frac{\rho_b}{\varepsilon_0} s_{Fe} \quad (1)$$

where c_{Fe} is the concentration of MZVI particles dispersed in the pore fluid [M L^{-3}], s_{Fe} is the concentration of retained MZVI particles (mass of iron per unit mass of porous medium) [M M^{-1}], ρ_b the bulk density of the porous medium [M L^{-3}], ε_0 is the initial porosity of the column [-].

The pressure drop was also monitored at column ends during the whole test with a time interval of 1 s (**Figure 2**), and was reported as the average gradient along the column of length L, $\Delta p/L = (p_{in}-p_{out})/L$.

2.4. MZVI transport modeling for column tests

The experimental results of column experiments were fitted using an extended formulation of E-MNM1D (Tosco and Sethi, 2010), which couples MZVI transport, porous medium clogging and non-Newtonian flow of the slurries.

The MZVI transport was modeled by a modified advection-dispersion-deposition equation (Tiraferri et al., 2011; Tosco and Sethi, 2010):

$$\frac{\partial}{\partial t}\left(\varepsilon c_{Fe}\right) + \sum_i \frac{\partial\left(\rho_b s_{Fe,i}\right)}{\partial t} + \frac{\partial}{\partial x}\left(q c_{Fe}\right) - \frac{\partial}{\partial x}\left(\varepsilon D_x \frac{\partial c_{Fe}}{\partial x}\right) = 0 \quad (2)$$

where ε is the porosity, D_x is the hydrodynamic dispersion coefficient [L^2 T^{-1}], and q is the Darcy velocity [L T^{-1}].

The source/sink term (second term of eq. (2)) represents the MZVI kinetic deposition onto and release from the solid matrix, and can be expressed by several formulations, depending on the processes involved, and several concurrent interaction sites, each representing a different process. When considering the injection of concentrated, meta-stable suspensions of particles, like MZVI slurries, the particles are expected to deposit in the pores and consequently to modify the hydrodynamic properties of the porous medium, namely permeability K and porosity ε, and the deposition and release kinetics. In this work two interaction sites were considered ($i = 1,2$), one (resulting in $s_{Fe,1}$) expressing linear deposition mechanisms formulated following the colloid filtration theory, and the other one (resulting in $s_{Fe,2}$) taking into account non-linear deposition processes which arise in concentrated and unstable suspensions:

$$\begin{cases} \dfrac{\partial\left(\rho_b s_{Fe,1}\right)}{\partial t} = \varepsilon k_{a,1} c_{Fe} - \rho_b k_{d,1} s_{Fe,1} \\ \dfrac{\partial\left(\rho_b s_{Fe,2}\right)}{\partial t} = \varepsilon k_{a,2}\left(1 + A_2 {s_{Fe}}^{B_2}\right) c_{Fe} - \rho_b k_{d,2} s_{Fe,2} \end{cases} \tag{3}$$

The total concentration of deposited particles, s_{Fe}, is the sum of the concentrations in phase 1 and 2, $s_{Fe} = s_{1,Fe} + s_{2,Fe}$. The first site is formulated following a linear reversible dynamics, where $k_{a,1}$ is the deposition rate [T^{-1}], and $k_{d,1}$ is the release rate [T^{-1}]. The second interaction site was modelled following the general formulation of deposition kinetics previously developed by the authors (Tosco and Sethi, 2010). A_2 [-] and B_2 [-] are two coefficients expressing how the concentration of deposited particles affects the removal rate on site 2. As a general rule, A_2 can be either negative (blocking dynamics, the deposition rate decreases with increasing the amount of particles already deposited) or positive (clogging site, the deposition rate increases with increasing s_{Fe}). In this application, the deposition rate is expected to increase with increasing s_{Fe}, due to the colloidal

instability of the suspension, with consequent porous medium clogging, as already observed in similar experimental conditions (Tosco et al., 2012; Tosco and Sethi, 2010). Therefore, here A_2 is assumed positive.

Straining was not considered as a removal mechanism, since the colloid diameter to pore size ratio in our system is equal to $3.9 \cdot 10^{-3}$, below the limit reported in the literature for the relevance of straining, namely $8 \cdot 10^{-3}$ (Xu et al., 2006).

In the classical formulation of the clean bed filtration theory, deposition is considered at its early stages, and detachment is not take into account. The attachment rate coefficient can be expressed as (Logan et al., 1995; Yao et al., 1971):

$$k_a = \frac{3}{2}(1-\varepsilon)\frac{v_e}{d_{50,sand}}\alpha_{att}\eta_0 \tag{4}$$

where v_e is the modulus of the effective velocity [L T^{-1}], η_0 is the single collector efficiency, given by the sum of the diffusion, interception and sedimentation processes, $\eta_0 = \eta_I + \eta_D + \eta_G$, and α_{att} is the collision efficiency [-] (Kretzschmar et al., 1999; Tufenkji and Elimelech, 2004). Several formulations are available for the calculation of the single collector efficiency, characterized by different degrees of complexity and number of phenomena considered in their formulation (Elimelech, 1992; Elimelech, 1995; Ngueleu et al., 2014; Rajagopalan and Tien, 1976; Tufenkji and Elimelech, 2004; Yao et al., 1971). In this work, the formulation of Yao (Yao et al., 1971) is selected for its simplicity (but also other formulations can be adopted):

$$\eta_I = \frac{3}{2}\left(\frac{d_{50,Fe}}{d_{50,sand}}\right)^2$$
$$\eta_D = 4.04 Pe^{-2/3} \quad (5)$$
$$\eta_G = \frac{v_s}{v_e}$$

where $d_{50,Fe}$ is the diameter of the colloidal particles [L], v_s is the sedimentation rate of the particles in the pore fluid [L T^{-1}], and Pe is the Peclet number [-]. The removal efficiency due to gravity was formulated by Yao in the hypothesis of vertical flow. However, it can be demonstrated (Supporting Information) that also in case of horizontal flow in a porous medium the particle removal due to sedimentation under gravity follows a first order kinetics, and the formulation of Yao can still be adopted. The sedimentation rate v_s is calculated using a modified Stokes law for non Newtonian fluids (see Appendix), which considers the actual viscosity of the suspension, that is, the shear dependent viscosity (Gastone et al., 2014).

The formulation of eq. (4) was here modified since the hypotheses under which it was derived are significantly different from those holding during MZVI transport (i.e. favourable deposition, single collector, no interaction with deposited colloids, no release, no concurrent phenomena, etc.) (Elimelech, 1994; Yao et al., 1971). In both sites, the collision efficiency and the porosity-dependent terms were lumped into a single coefficient, named $C_{a,i}$ [-] ($i=1,2$), to be heuristically determined from the fitting of the experimental data, and therefore the attachment rates $k_{a,i}$ of eq. (3) are here expressed as:

$$k_{a,i} = C_{a,i} \frac{v_e}{d_{50,sand}} \eta_0 \quad (6)$$

The attachment rate in the second site was further modified to take into account the colloidal instability of the concentrated MZVI suspensions, including a dependence on the concentration of deposited particles. The concentration-dependent term in eq. (3), $1+A_2 s_{Fe}^{B_2}$, increases the removal rate with increasing deposited concentration s_{Fe}, and reflects the progressive reduction in the average travel path of the particles in the pores due to the accumulation of the deposits, which in turn reduce the pore space and cause partial clogging of the smallest pores.

Finally, detachment was included, as formulated in eq. (3), to represent the possible shear detachment of MZVI particles retained on portions of the sand grains accessible to fluid flow. Li et al. (2005) proved with experimental results that a direct dependence of the detachment rate on the drag force exists, observing a proportionality between detachment and flow velocity, and therefore the drag force was calculated as the product of viscosity, effective velocity, and shape-dependent parameters. Other authors reported a power dependence of the detachment coefficients on the drag force, with exponents lower than 1 (Brovelli et al., 2009). Moreover, an estimate of the conditions for rolling, lifting and consequent detachment of retained particles can be obtained based on torque balance of the forces acting on the particles (namely, drag, lifting, electrostatic and gravity forces) (Bedrikovetsky et al., 2011; Bergendahl and Grasso, 2000; Bradford and Torkzaban, 2008; Johnson and Hilpert, 2013), showing also in this case a direct proportionality of detachment to viscosity and pore velocity. Even though the conditions in which the tests in the study of Li et al. (2005) and the cited approaches based on torque balance were performed are significantly different (Newtonian fluid, diluted colloidal suspension, unfavourable deposition conditions, etc.), we assume here that the direct proportionality between the detachment rate and the drag force holds also for MZVI

transport. Since an analytical computation of the drag force is rather complex for our experimental conditions, the dependence of the detachment rate on drag was modelled as

$$k_{d,i} = C_{d,i}\mu_m v_e \tag{7}$$

where $C_{d,i}$ [T M^{-1}] is an empirical parameter to be determined from fitting of the experimental data, and μ_m [M L^{-1} T^{-1}] is the shear thinning viscosity of the slurry, which depends on the flow velocity and guar gum concentration and is here calculated as discussed in the companion paper Part I (see detailed equations in the Appendix).

The reduction of K and ε due to MZVI deposition was modelled following the approach previously proposed by the authors (Tosco and Sethi, 2010). For MZVI dispersed in guar gum solutions, two concurrent processes contribute to the porous medium clogging, namely the mechanical filtration of residual undissolved guar gum particles and the retention of MZVI. The filtration of residual solid particles of guar gum was modelled as a linear irreversible retention, using the relationships and parameters discussed in the companion paper Part I (equations are reported in the Appendix). A retention kinetics k_{ap} of $6.3 \cdot 10^{-3}$ s^{-1} was obtained in Part I for the guar gum solutions used in this study.

The pressure build up arising from the injection of the non-Newtonian slurry of MZVI was calculated using a modified formulation of the Darcy's law (Tosco et al., 2013), which takes into account both the reduction in permeability, and the shear thinning nature of the fluid, following the same approach adopted in Part I for the flow of guar gum solutions without MZVI particles:

$$-\nabla p = \frac{\mu_m(\dot{\gamma}_m)}{K} q \tag{8}$$

where the fluid viscosity μ_m depends on the shear rate in the porous medium $\dot{\gamma}_m$, and the permeability K is declining with increasing concentration of deposited particles of guar gum (s_P) and MZVI (s_{Fe}):

$$\begin{cases} K = \left(\dfrac{\varepsilon}{\varepsilon_0}\right)^3 \left(\dfrac{a_0}{a}\right)^2 K_0 \\ \varepsilon = \varepsilon_0 - \dfrac{\rho_b}{\lambda_{Fe}\rho_{Fe}} s_{Fe} - \dfrac{\rho_b}{\lambda_p \rho_p} s_p \\ a = a_0 + a_{Fe}\dfrac{\rho_b}{\rho_{Fe}} s_{Fe} + a_p \dfrac{\rho_b}{\rho_p} s_p \end{cases} \quad (9)$$

The whole set of equations is reported in the Appendix. A more detailed discussion on clogging effects of the filtration of guar gum residual particles is reported in the companion paper Part I.

The flow and transport equations were fitted to the experimental data of column transport tests using a modified version of E-MNM1D (Tosco and Sethi, 2010). A graphical interface for E-MNM1D is provided by the software MNMs, which is available for download at www.polito.it/groundwater/software.

The parameters of the viscosity model $\mu_m(\dot{\gamma}_m)$ (eq. A2-A3 in the Appendix) and of the clogging due to guar gum (eq. 9) were determined in Part I from guar gum filtration tests. The transport and clogging parameters related to MZVI transport were obtained from the fitting of the MZVI column transport tests presented here in Part II, and included the degree of packing of the deposits of iron particles λ_{Fe} [-], the specific surface of the deposits a_{Fe} [L^{-1}], the coefficients of the clogging site A_2 and B_2, the deposition and release coefficients α'_{att}, $k_{d,1}$ and $k_{a,2}$.

All tests were fitted against the model equations simultaneously, since some parameters (λ_{Fe}, a_{Fe}, A_2 and B_2,) were assumed constant for all tests, while others (α'_{att} and $k_{a,2}$) were allowed to change

from test to test, in order to highlight further dependences on specific variables (namely, flow velocity, sedimentation rate, viscosity). In particular, $k_{a,2}$ and $k_{a,2}$ were fitted on each test and then reported as a function of $v_s/d_{50,sand}.\eta_0$ in order to verify the correctness of the assumptions behind the formulations of eq. (6), while $k_{d,1}$ was fitted for each test and reported as a function of μ_m and v_e in order to verify eq. (7).

2.5. Flow and transport simulation in radial domains

The experimental and modeling results of column tests provided the relationships for the dependence of the transport parameters on the flow velocity. They were then included in the radial formulation of the transport model, and the transport of MZVI was then simulated in a radial symmetric field, which is representative of a field application using an injection well. The steps of the model development and the model equations are summarized respectively in **Figure 4** and in the Appendix.

In a radial flow field, the Darcy velocity q is not constant any more with increasing radial distance r, but declines hyperbolically with r (**Figure 1**):

$$q = \frac{Q}{2\pi r b} \tag{10}$$

where Q is the discharge rate [L^3 T^{-1}], and b is the well screen thickness [L].

Consequently, in full-scale applications the flow velocity and all velocity-dependent parameters are not constant over the entire domain any more.

The transport equation becomes

$$\frac{\partial}{\partial t}(\varepsilon c_{Fe}) + \sum_i \frac{\partial(\rho_b s_{Fe,i})}{\partial t} + \frac{1}{r}\frac{\partial}{\partial r}(rqc_{Fe}) - \frac{1}{r}\frac{\partial}{\partial r}\left[r\varepsilon D_r \frac{\partial c_{Fe}}{\partial r} \right] = 0 \qquad (11)$$

In a radial flow field, deposition and release mechanisms as well as porous medium clogging can be modeled using the same equations presented for the 1D Cartesian domain (eq. (3-10)).

The transport model was implemented in radial geometry and used in forward mode to simulate different scenarios of full-scale applications. First, illustrative simulations reproducing the guar gum concentrations applied in column transport tests were run, assuming a particle concentration of 20 g/l, guar gum concentrations of 1.5, 3 and 4 g/l, discharge rate of 1 m^3/h per unit length of the well screen, for a total injection time of 5 h. A well diameter of 0.52 m was assumed. The model domain ranged from the outer limit of the well drain (r_0 = 0.26 m) to a radial distance of 5 m. The domain was discretized in 170 cells, with size logarithmically increasing with radial distance. Second, a set of simulations were run exploring the combined influence of guar gum concentration (1.5 to 7 g/l) and discharge rate (0.25 to 5 m^3/h) on the pressure build up and radius of influence for a target concentration of 5 g/l, which was selected as representative of the typical range of concentrations in field applications of injectable zerovalent iron (Henn and Waddill, 2006; O'Carroll et al., 2013; Tosco et al., 2014; Yan et al., 2013)

An initial condition of model domain fully saturated with water was assumed, with no background flow rate. Boundary conditions of first-order constant concentration at the inlet, second-order zero gradient at the outlet were imposed. Aquifer properties (porosity, permeability, bulk density, average grain size, etc.), slurry properties (viscosity model, sedimentation rate, etc.) and deposition/release kinetics were assumed equal to those of the sand-packed columns.

3. Results and discussion

3.1. Column transport tests

3.1.1. Experimental results

The experimental results of column transport tests for MZVI particles (20 g/l) dispersed in guar gum solutions (1.5, 3 and 4 g/l) are reported in **Figure 5** to **Figure 7**, in terms of breakthrough curves (**Figure 5**), average pressure gradient along the column (**Figure 6**) and profiles of total iron (**Figure 7**). The breakthrough curves indicate that higher polymer concentration and higher flow velocity improve the mobility of the particles, resulting in a breakthrough above 90% at 0.4 m. Conversely, lower concentrations of guar gum result in less stable suspensions, and consequently in lower breakthrough. Mass balances (**Table 1**) indicate that, in all experimental conditions except two, at least 50% of the injected MZVI reached the outlet of the column after flushing. In most cases, the breakthrough is 70% or higher.

Two concurrent retention mechanisms can be inferred from a qualitative observation of the breakthrough curves. The first is likely to be a reversible mechanism, and dominates for fairly stable suspensions: in this case (all tests at 4 g/l in **Figure 5**c, and the tests at $q_4 = 1.9 \cdot 10^{-3}$ and $q_2 = 4.4 \cdot 10^{-4}$ at 3 g/l, **Figure 5**b) the increase in the breakthrough concentration is moderately sharp in the early stages of the injection, indicating that a dynamic deposition and release is occurring. For longer times, an almost steady state outlet concentration is reached, lower than the injected one

($C/C_0<1$) but significantly high. Finally, during flushing a significant tailing is observed, associated to the release of reversibly retained particles (see in particular **Figure 5**c).

The second retention mechanism is associated to irreversible deposition, and is more pronounced for less stable suspensions (1.5 g/l of guar gum, **Figure 5**a, and 3 g/l of guar gum at $q_1 = 1.0 \cdot 10^{-4}$ *m/s*, **Figure 5**b), which have a sedimentation half time close to or lower than the pore volume time (**Table 1**). All breakthrough curves reach a steady state concentration lower than one, indicating that an equilibrium is not reached. The less stable the colloidal suspension, the more pronounced is the phenomenon. Moreover, in two cases (1.5 g/l at $q_2 = 4.3 \cdot 10^{-4}$ *m/s*, **Figure 5**a, and 3 g/l at $q_1 = 1.1 \cdot 10^{-4}$ *m/s* **Figure 5**b) after the initial steep increase in the breakthrough concentration, a subsequent decline is observed, which is typical of filter ripening, and in general of pronounced non linear deposition (Hosseini and Tosco, 2013; Tiraferri and Sethi, 2009; Tosco et al., 2012), suggesting that the retention is increasing with the injection time. For these tests, the tailing in the breakthrough curve during flushing is short, confirming that most particles are irreversibly retained. This is in agreement with concentration profiles before and after flushing (**Figure 7**) and mass balances (**Table 1**): profiles for more stable suspensions are lower (that is, less particles are retained), less steep (the iron distribution is more homogeneous inside the column) and exhibit a more pronounced reduction in retained iron after flushing, indicating that a significant fraction of the particles retained at the end of the injection phase is then re-mobilized during flushing. Conversely, less stable suspensions have higher concentrations of retained particles, coherently with the breakthrough curves, steeper profiles, and exhibit a limited difference between profiles pre- and post-flushing, which confirms that the particles are irreversibly retained.

Under the hypothesis of steady state outlet concentration, negligible dispersion, one linear irreversible site following eq. (6), the mass balance eq. (2) for the liquid phase reduces to

$$\varepsilon C_a \frac{v_e}{d_{50,sand}} \eta_0 c + \frac{\partial}{\partial x}(q c_{Fe}) = 0 \qquad (12)$$

which can be integrated between the entrance ($x=0$) and exit ($x=L$) of the column, leading to

$$\frac{c_{Fe}(L)}{c_{Fe,0}} = \exp\left(- C_a \frac{L}{d_{50,sand}} \eta_0 \right) \qquad (13)$$

Eq. (13) is derived under the assumption of steady state transport and negligible reduction of porosity due to retention of particles (Yao et al., 1971), and can provide a first estimate of the expected breakthrough concentration for fairly stable suspensions. However, in case of concentrated, poorly stable suspensions and prolonged injection, the hypothesis of negligible reduction of porosity fails, and therefore eq. (13) does not hold any more. In this case, the implementation of the complete transport equations, including the ripening formulation of eq. (4), site 2, is necessary.

Figure 8a reports the maximum (steady state) outlet concentration for all tests and duplicates as a function of the removal efficiency η_0 calculated as the sum of the terms in eq. (5). For low to intermediate removal efficiency, it can be observed that the experimental points are fairly aligned, while for higher removal efficiencies the points diverge towards lower values (compare the four points on the right of the plot, corresponding to 3 g/l and 1.5 g/l of guar gum injected at the lowest flow rate). The reason of this divergence from the simple model of clean bed filtration can be attributed to the limited colloidal stability of the MZVI dispersion in these tests. Comparing with

Table 1, it can be seen that these tests correspond to a ratio of sedimentation half time t_s (i.e. the time in which half the particles are expected to sediment in the porous medium) to breakthrough time of the column (t_{PV}) significantly lower than 1, that is, to those tests in which the suspension is less stable. Eq. (13) does not fit well the entire set of data. Conversely, if eq. (13) is fitted to the experimental points in **Figure 8**a which correspond to a ratio t_s/t_{PV} equal to or higher than 1, then the fitting is satisfactory (see black line in **Figure 8**a, obtained for $C_a = 1.07$). **Figure 8**b reports, for each test (including duplicates), the three terms of the removal efficiency η_0, showing that sedimentation is the predominant removal mechanism for the three abovementioned tests.

MZVI retention during injection also results in a progressive decline of permeability, as reflected by the evolution of pressure gradient over time (**Figure 6**). The pressure drop at column ends increases with time due to the concurrent deposition of iron particles and guar gum solid residuals, as discussed in Part I. The porous medium plugging gives rise to an almost linear increase of the pressure gradient with time. Less stable suspensions (3 g/l of guar gum injected at $q_1 = 1.0 \cdot 10^{-4}$ *m/s*, and 1.5 g/l guar gum injected at $q_2 = 4.3 \cdot 10^{-4}$ *m/s*) result in a super-linear increase with time, which would lead to the complete clogging of the medium if the injection were prolonged further.

3.1.2. 1D modeling

The experimental data of breakthrough concentration c_{Fe}, pressure drop evolution $\Delta p/L$, and profiles of total iron retained in the column s_{Fe} were fitted to the model eq. (2-11), in order to determine the parameters controlling the MZVI transport and the associated clogging of the porous medium. The two interaction mechanisms discussed in the previous paragraph, namely reversible deposition and irreversible retention associated to MZVI colloidal instability, were modeled respectively by site 1

and site 2 in eq. (3). Consequently, in this study $k_{d,2}$ was assumed equal to 0. The fitted curves are reported in **Figure 5**, **Figure 6** and **Figure 7** along with the experimental data.

It can be observed that during MZVI injection the model correctly reproduces the shape of the experimental breakthrough curves, concentration profiles and pressure curves. Conversely, during flushing the agreement is less satisfactory. This can be attributed to the mechanisms controlling the displacement of the MZVI slurry by water (Ciriello and Di Federico, 2012). Being water less viscous that the slurry, the so called miscible displacement takes place, that is, the water flows through the largest pores and in the center of them, and a residual saturation of guar gum slurry remains "attached" to the porous medium grains, similarly to what happens in case of multiphase flow, as discussed more in details in Part I. The process is not observed when the displacing fluid is the most viscous one (that is, at the beginning of MZVI injection), and consequently the first part of the tests is correctly described by the model. The flow and transport model herein adopted, based on E-MNM1D, does not incorporate incomplete miscible displacement, and consequently the flushing step cannot be fully depicted. However, this phenomenon is not expected to be relevant when simulating a field-scale injection of MZVI, since in real applications the slurry injection is not usually followed by a further water injection, and consequently the process is beyond the scope of this study.

The flow and transport parameters determined by the fitting of the experimental data are reported in **Table 2**. A single value was fitted for the parameters controlling the impact of particles retained on the permeability (eq. A10), and consequently on the pressure drop (a_{Fe} and λ_{Fe}). The good fitting of the pressure drop curves (**Figure 6**) indicates that the hypothesis of independence of a_{Fe} and λ_{Fe} on flow velocity and guar gum concentration was correct. The same for the coefficients A_2 and B_2

controlling how the presence of retained particles influence the deposition rate of the second site (eq. 3).

The attachment coefficients $k_{a,1}$ and $k_{a,2}$ were determined for each test. The formulation of the attachment kinetics as a function of the retention efficiency η_0 (eq. 6) was verified reporting the fitted values of $k_{a,2}$ against the group $v_e/d_{50,sand}\cdot\eta_0$ (function of guar gum concentration and flow velocity). A clear linear trend is found in both cases (**Figure 9**a and c), indicating that formulation of eq. (6) was correct. The least-squares fitting of the coefficients $k_{a,1}$ and $k_{a,2}$ with eq. (6) is reported in **Figure 9**a and c as black lines. Also for the detachment coefficient $k_{d,1}$ a linear trend is observed when it is reported as a function of $\mu_m\cdot v_e$ (**Figure 9**b), confirming that the assumption of linear proportionality between detachment rate $k_{d,1}$ and drag force (eq. (6)) is correct.

In summary, the following relationships, which will be used in the development of the radial model, are proposed for the attachment and detachment rates as functions of pore fluid viscosity μ_m and velocity v_e:

$$\begin{cases} k_{a,1}(\mu_m, v_e) = C_{a,1}\dfrac{v_e}{d_{50,sand}}\eta_0\big|_{Yao}(\mu_m, v_e) \\ k_{d,1}(\mu_m, v_e) = C_{d,1}\mu_m v_e \\ k_{a,2}(\mu_m, v_e) = C_{a,2}\dfrac{v_e}{d_{50,sand}}\eta_0\big|_{Yao}(\mu_m, v_e) \end{cases} \tag{14}$$

The numerical values of the parameters determined from the least-squares fitting are $C_{a,1}$ = 2.01 (-) (**Figure 9**a), $C_{d,1}$ = 31.35 s/kg (**Figure 9**b), and $C_{a,2}$ = 0.78 (-) (**Figure 9**c).

3.2. Simulations of radial injection of MZVI

The eq. (14) expressing the dependence of the transport parameters on the flow velocity and shear thinning viscosity were implemented in a transport and flow model, solving the eq. (2-12) in a radial symmetric geometry, which can be assumed as a simplified representation of a full-scale injection through a well.

Examples of forward model runs are reported in **Figure 10**. The simulations were performed assuming a discharge rate of 1 m^3/h for 5 h, for a total injected volume of 5 m^3. The hyperbolic decrease of Darcy velocity for the applied discharge with radial distance is reported in **Figure 1**. The positions corresponding to the four flow rates explored in the column tests fall within the first meter of the model domain. In particular, q_4, q_3 and q_2 are representative of the vicinity or close vicinity to the injection well, while q_1 is representative of longer distances. Coherently, the viscosity of the guar gum solution also significantly varies with increasing radial distance, even in the absence of any clogging process, due to its dependence on the flow velocity, as discussed in the companion paper Part I.

The radius of influence of the injection, *ROI*, can be defined as the maximum radial distance where the total iron concentration $c_{tot,Fe}$ is equal to or lower than a fixed target concentration, which is to be determined based on reactivity tests. Here a limit concentration of 5 g/l was assumed for all simulations. **Figure 10** reports the evolution over space and time of the iron concentration, both for suspended iron c_{Fe} and total iron $c_{tot,Fe}$ (calculated using eq. (1)), for guar gum concentration of 1.5, 3 and 4 g/l. The simulation results indicate that the highest mobility is obtained for particles dispersed in 4 g/l guar gum solutions, with a radius of influence close to 2 m after 5 hours of injection (**Figure 10**c,f). A slightly shorter radius of influence (1.5 m) is also obtained after 5 h for the slurry at 3 g/l of guar gum (**Figure 10**b,e), even though in this case most iron particles are

retained closer to the injection well, with a less homogeneous iron distribution within the domain. Conversely, for 1.5 g/l of guar gum (**Figure 10**a,d), the particles are retained within 0.7 m from the well. Moreover, the lower the guar gum concentration, the more particles are retained in high concentration close to the injection well, giving rise to an extremely inhomogeneous distribution of the particles. This finding can be attributed to the very high flow velocities experienced in the immediate vicinity of the injection well, which result in a reduced viscosity of the pore fluid, and consequently in fast sedimentation of the particles. This phenomenon could be partly overcome using wells and drain packs of larger size, even though this could lead to other practical problems in the field (eg. large well volume, risk of particle sedimentation in the well, etc.).

The results of **Figure 10** and **Figure 11** show the influence of the injection time on the overall radius of influence and on the iron distribution. When the suspension is fairly stable (c_{GG} = 4 g/l in particular, and c_{GG} = 3 g/l to some extent), increasing the injection time results in an increased radius of influence, even though there is no linear proportionality, since larger distances correspond to larger volumes of aquifer. On the contrary, if the suspension is not very stable (in particular for c_{GG} = 1.5 g/l) increasing the injection time does not result in a significant increase in the radius of influence, but only in an increase of the concentration of deposited particles within the same portion of the aquifer (**Figure 10**a,d).

The accumulation of particles close to the injection well, where flow velocity is higher, also results in a progressive clogging of the porous medium. **Figure 12** reports the total pressure in the model domain, which is calculated as the integral of pressure gradient along the radial distance:

$$\Delta P_{tot} = \int_{r_w}^{r_{out}} p dr \qquad (14)$$

where r_w is the radius of the well (inner boundary of the model domain) and r_{out} is the outer boundary of the model domain (i.e. where pressure build up goes to zero, here equal to 3 m).

From a practical point of view, this pressure corresponds to the pressure which is to be applied at the well during injection to keep the discharge rate constant.

The contribution to the overall injection pressure due to iron is highlighted in **Figure 12**, which reports, for the three values of guar gum concentration, the total pressure ΔP_{tot} which would be generated injecting only dissolved guar gum, without iron nor solid polymeric residuals (dotted lines), and which is due to the viscosity of guar gum; the ΔP_{tot} which would be generated by guar gum, with polymeric residual particles dissolved in it (dashed lines), as discussed in Part I for column filtration tests; and the ΔP_{tot} generated by both dissolved and residual guar gum along with iron particles. The plot indicates that, for fairly stable suspensions (4 g/l and 3 g/l of guar gum), the pressure build up increases moderately with time, and is mainly determined by the viscosity of the slurry. The additional contributions due to undissolved guar gum which is retained in the porous medium and deposited iron are limited. Conversely, for unstable suspensions (1.5 g/l) the pressure build up increases significantly with time, and the porous medium is progressively clogged. Except for the initial stages, the pressure build up is predominantly due to retained iron, and an exponential increase is observed in the advanced stages of the injection. From the point of view of the iron mobility, this corresponds to a substantially constant radius of influence. After approximately two hours, the pressure build up starts increasing sharply, indicating that a relevant clogging is occurring. In these conditions, further injecting iron slurry does not result in any significant increase of the radius of influence (**Figure 11**), but only in a further accumulation of particles in the close vicinity of the well, and in a corresponding fast increase in the pressure build up. If the injection is

further prolonged, in real conditions a fracturing of the porous medium is likely to occur when ΔP_{tot} overcomes the critical pressure of the aquifer system. As a consequence, a plot similar to **Figure 12** can be useful in the preliminary design of a field injection, comparing the simulated pressure build up to the expected critical pressure of the aquifer.

Forward simulations in the radial domain like those reported as an example in this paragraph can be also used as a tool for an assisted preliminary design of full scale injection of MZVI slurries. To this aim, forward simulations were run varying discharge rate Q (0.25 to 5 m^3/h) and guar gum concentration c_{GG} (1.5 to 7 g/l), simulating the injection of 5 m^3 of 20 g/l MZVI slurry. 20 values of Q and 20 values of c_{GG} were considered, for a total number of 400 possible combinations (and corresponding total runs). The results were processed in order to obtain the final pressure build up ΔP_{tot} and the radius of influence ROI for a target concentration of 5 g/l in each condition, and the results are reported in **Figure 13**. The plots indicate that increasing guar gum concentration and increasing discharge rate both result in an increase in pressure build up (**Figure 13**a). The same is observed for the ROI (**Figure 13**b). However, in this case the plot also indicates that, in case of low guar gum concentration, and therefore of poorly stable MZVI suspensions, increasing the discharge rate (with a proportional decrease in the total injection time, since the total volume of slurry is constant in all simulations) results in a very limited increase of the ROI, while the pressure build up significantly increases (compare to **Figure 13**a). Conversely, high guar gum concentrations can result in significantly high radii of influence, even though in this case the pressure build up can be the limiting factor. As a general rule, a compromise between good mobility and limited overpressure is obtained for medium to high guar gum concentrations and intermediate discharge rates.

The isoline corresponding to the critical pressure of the aquifer can be reported in the plot of ΔP_{tot}, identifying the range of guar gum concentrations and discharge rates which are compatible with permeation injection. On the other hand, the minimum desired *ROI* identifies another region on the plot on the *ROI* map. The superposition of the two plots identifies the possible combinations of guar gum concentration and discharge rate which satisfy the operational constraints.

4. Conclusions

In this paper and in the companion publication Part I, a systematic study on the use of guar gum solutions in the injection of MZVI particles for groundwater remediation was developed. The radial model E-MNM1R herein presented can provide useful information for the design of a full scale injection of MZVI. It is worth to mention that, even if the model is based on transport equations and semi-empirical relationships derived from or validated against experimental data at the laboratory scale, at the moment a validation against experimental data of a field-scale injection is not available, and represents an important step for the future development of the work, and for the reliable application of the model for a fully quantitative prediction of MZVI mobility at the large scale.

Graphs like those reported in **Figure 11** to **Figure 13** can be used as semi-quantitative tools for an assisted design of a field injection. Such plots are site-specific, and strongly influenced by the hydrodynamic and hydrochemical properties of the aquifer system, as well as by the rheology of the slurry, iron particle size, concentration etc. Moreover, in its formulation the model herein presented

does not take into account possible hydrodynamic and hydrochemical heterogeneities, which may even significantly influence both flow and MZVI retention kinetics and mechanisms.

A deeper analysis of graphs like those of **Figure 11** to **Figure 13** also suggest that, when designing a field injection, several concurrent aspects are to be taken into account, and the radius of influence cannot be the only design parameter. The overpressure induced by the slurry injection can be in many cases the most critical aspect, in particular when injecting at shallow depths. In this case the critical pressure of the aquifer system is limited, and can be more easily overcome, thus resulting in the formation of preferential flow paths and, in the most critical situations, in the daylighting of the injected slurry. Even though a high concentration of the thickening agent helps improving the overall colloidal stability of the slurry, it also significantly increases the slurry viscosity and consequently the injection pressure. Also the presence of residual undissolved guar gum particles, and, more in general, of any impurity present in the dispersing fluid can have a negative impact on the overall injection pressure. In this sense, a careful design of the iron slurry is a fundamental aspect, in order to limit as much as possible the presence of undissolved materials, and to define the minimum polymer concentration which provides a stable suspension for the envisioned duration of the field injection.

Based on the considerations reported above, it can be concluded that the design of a field injection of stabilized MZVI, and more in general, of any colloidal suspension of reactive material requires a careful evaluation of concurrent aspects, ranging from the selection of particle type and size up to the definition of the discharge rate, and including both experimental and modeling steps, at different scales, among which transport simulations are a key point. The radial transport model herein presented can represent a valid tool in this sense.

Acknowledgement

The work was co-funded by the EU research project AQUAREHAB (FP7, Grant Agreement n. 226565).

References

Abdel-Salam, A. and Chrysikopoulos, C.V., 1995. Modeling of colloid and colloid-facilitated contaminant transport in a two-dimensional fracture with spatially variable aperture. Transport in Porous Media, 20(3): 197-221.

Auset, M. and Keller, A.A., 2004. Pore-scale processes that control dispersion of colloids in saturated porous media. Water Resources Research, 40(3).

Bear, J., 1988. Dynamics of fluids in porous media. Dover books on physics and chemistry. Dover, New York, xvii, 764 p. pp.

Bedrikovetsky, P., Siqueira, F., Furtado, C. and Souza, A., 2011. Modified Particle Detachment Model for Colloidal Transport in Porous Media. Transport in Porous Media, 86(2): 353-383.

Berge, N.D. and Ramsburg, C.A., 2009. Oil-in-water emulsions for encapsulated delivery of reactive iron particles. Environmental Science and Technology, 43(13): 5060-5066.

Bergendahl, J. and Grasso, D., 2000. Prediction of colloid detachment in a model porous media: hydrodynamics. Chemical Engineering Science, 55(9): 1523-1532.

Bradford, S.A. and Torkzaban, S., 2008. Colloid Transport and Retention in Unsaturated Porous Media: A Review of Interface-, Collector-, and Pore-Scale Processes and Models All rights reserved. No part of this periodical may be reproduced or transmitted in any form or by any means, electronic or mechanical, including photocopying, recording, or any information storage and retrieval system, without permission in writing from the publisher. Vadose Zone J., 7(2): 667-681.

Brovelli, A., Malaguerra, F. and Barry, D.A., 2009. Bioclogging in porous media: Model development and sensitivity to initial conditions. Environmental Modelling & Software, 24(5): 611-626.

Chang, M.C., Shu, H.Y., Hsieh, W.P. and Wang, M.C., 2005. Using nanoscale zero-valent iron for the remediation of polycyclic aromatic hydrocarbons contaminated soil. Journal of the Air & Waste Management Association, 55(8): 1200-1207.

Chrysikopoulos, C.V. and Syngouna, V.I., 2014. Effect of gravity on colloid transport through water-saturated columns packed with glass beads: Modeling and experiments. Environmental Science & Technology, doi: 10.1021/es501295n.

Ciriello, V. and Di Federico, V., 2012. Similarity solutions for flow of non-Newtonian fluids in porous media revisited under parameter uncertainty. Advances in Water Resources, 43(0): 38-51.

Comba, S., Dalmazzo, D., Santagata, E. and Sethi, R., 2011. Rheological characterization of xanthan suspensions of nanoscale iron for injection in porous media. Journal of Hazardous Materials, 185(2–3): 598-605.

Dalla Vecchia, E., Coisson, M., Appino, C., Vinai, F. and Sethi, R., 2009a. Magnetic Characterization and Interaction Modeling of Zerovalent Iron Nanoparticles for the

Remediation of Contaminated Aquifers. Journal of Nanoscience and Nanotechnology, 9(5): 3210-3218.

Dalla Vecchia, E., Luna, M. and Sethi, R., 2009b. Transport in Porous Media of Highly Concentrated Iron Micro- and Nanoparticles in the Presence of Xanthan Gum. Environmental Science & Technology, 43(23): 8942-8947.

Di Molfetta, A. and Sethi, R., 2006. Clamshell excavation of a permeable reactive barrier. Environmental Geology.

Elimelech, M., 1992. Predicting collision efficiencies of colloidal particles in porous media. Water Research, 26(1): 1-8.

Elimelech, M., 1994. Effect of Particle Size on the Kinetics of Particle Deposition under Attractive Double Layer Interactions. Journal of Colloid and Interface Science, 164(1): 190-199.

Elimelech, M., 1995. Particle deposition and aggregation : measurement, modelling, and simulation. Colloid and surface engineering series. Butterworth-Heinemann, Oxford England ; Boston, xv, 441 p. pp.

Elliott, D.W., Cao, J.S., Zhang, W.X. and Spear, S.T., 2003. Degradation of aaueous hexachlorocyclohexanes by iron nanoparticles. Abstracts of Papers of the American Chemical Society, 225: U803-U803.

Elliott, D.W. and Zhang, W.X., 2003. Field assessment of nanoscale bimetallic particles for groundwater treatment. Abstracts of Papers of the American Chemical Society, 225: U971-U971.

Fatisson, J., Ghoshal, S. and Tufenkji, N., 2010. Deposition of carboxymethylcellulose-coated zero-valent iron nanoparticles onto silica: Roles of solution chemistry and organic molecules. Langmuir, 26(15): 12832-12840.

Freyria, F.S., Bonelli, B., Sethi, R., Armandi, M., Belluso, E. and Garrone, E., 2011. Reactions of acid orange 7 with iron nanoparticles in aqueous solutions. Journal of Physical Chemistry C, 115(49): 24143-24152.

Gastone, F., Tosco, T. and Sethi, R., 2014. Green stabilization of microscale iron particles using guar gum: bulk rheology, sedimentation rate and enzymatic degradation. Journal of Colloid and Interface Science, 421: 33-43.

Hadnagy, E., Gardner, K.H., Spear, J.M., Aulisio, D. and Calante, I., 2004. In situ PCB dechlorination in sediments using nanoscale and microscale zero-valent iron. Abstracts of Papers of the American Chemical Society, 228: U601-U601.

He, F. and Zhao, D.Y., 2005. Preparation and characterization of a new class of starch-stabilized bimetallic nanoparticles for degradation of chlorinated hydrocarbons in water. Environmental Science & Technology, 39(9): 3314-3320.

Henn, K.W. and Waddill, D.W., 2006. Utilization of nanoscale zero-valent iron for source remediation—A case study. Remediation Journal, 16(2): 57-77.

Hosseini, S.M. and Tosco, T., 2013. Transport and retention of high concentrated nano-Fe/Cu particles through highly flow-rated packed sand column. Water Research, 47(1): 326-338.

Johnson, R.L., Nurmi, J.T., O'Brien Johnson, G.S., Fan, D., O'Brien Johnson, R.L., Shi, Z., Salter-Blanc, A.J., Tratnyek, P.G. and Lowry, G.V., 2013. Field-Scale Transport and Transformation of Carboxymethylcellulose-Stabilized Nano Zero-Valent Iron. Environmental Science & Technology, 47(3): 1573-1580.

Johnson, W.P. and Hilpert, M., 2013. Upscaling colloid transport and retention under unfavorable conditions: Linking mass transfer to pore and grain topology. Water Resources Research: n/a-n/a.

Joo, S.H., Feitz, A.J. and Waite, T.D., 2004. Oxidative degradation of the carbothioate herbicide, molinate, using nanoscale zero-valent iron. Environmental Science & Technology, 38(7): 2242-2247.

Kanel, S.R., Nepal, D., Manning, B. and Choi, H., 2007. Transport of surface-modified iron nanoparticle in porous media and application to arsenic(III) remediation. Journal of Nanoparticle Research, 9(5): 725-735.

Keller, A.A., Sirivithayapakorn, S. and Chrysikopoulos, C.V., 2004. Early breakthrough of colloids and bacteriophage MS2 in a water-saturated sand column. Water Resources Research, 40(8): W08304.

Kocur, C.M., O'Carroll, D.M. and Sleep, B.E., 2013. Impact of nZVI stability on mobility in porous media. Journal of Contaminant Hydrology, 145: 17-25.

Kretzschmar, R., Borkovec, M., Grolimund, D. and Elimelech, M., 1999. Mobile subsurface colloids and their role in contaminant transport. Advances in Agronomy, Vol 66, 66: 121-193.

Leij, F.J. and Bradford, S.A., 2013. Colloid transport in dual-permeability media. Journal of Contaminant Hydrology, 150(0): 65-76.

Li, X., Zhang, P., Lin, C.L. and Johnson, W.P., 2005. Role of Hydrodynamic Drag on Microsphere Deposition and Re-entrainment in Porous Media under Unfavorable Conditions. Environmental Science & Technology, 39(11): 4012-4020.

Lien, H.L. and Zhang, W.X., 2001. Nanoscale iron particles for complete reduction of chlorinated ethenes. Colloids and Surfaces a-Physicochemical and Engineering Aspects, 191(1-2): 97-105.

Liu, Y.Q., Majetich, S.A., Tilton, R.D., Sholl, D.S. and Lowry, G.V., 2005. TCE dechlorination rates, pathways, and efficiency of nanoscale iron particles with different properties. Environmental Science & Technology, 39(5): 1338-1345.

Logan, B.E., Jewett, D.G., Arnold, R.G., Bouwer, E.J. and O'Melia, C.R., 1995. Clarification of clean-bed filtration models. Journal of Environmental Engineering, 121(12): 869-873.

Longo, S., Di Federico, V., Archetti, R., Chiapponi, L., Ciriello, V. and Ungarish, M., 2013. On the axisymmetric spreading of non-Newtonian power-law gravity currents of time-dependent volume: An experimental and theoretical investigation focused on the inference of rheological parameters. Journal of Non-Newtonian Fluid Mechanics, 201(0): 69-79.

Lowry, G.V. and Johnson, K.M., 2004. Congener specific dechlorination of dissolved PCBs by nanoscale zero-valent iron at ambient pressure and temperature. Abstracts of Papers of the American Chemical Society, 228: U607-U607.

Ngueleu, S.K., Grathwohl, P. and Cirpka, O.A., 2014. Particle-Facilitated Transport of Lindane in Water-Saturated Tropical Lateritic Porous Media. J. Environ. Qual., 0(0): -.

Nurmi, J.T., Tratnyek, P.G., Sarathy, V., Baer, D.R., Amonette, J.E., Pecher, K., Wang, C.M., Linehan, J.C., Matson, D.W., Penn, R.L. and Driessen, M.D., 2005. Characterization and properties of metallic iron nanoparticles: Spectroscopy, electrochemistry, and kinetics. Environmental Science & Technology, 39(5): 1221-1230.

O'Carroll, D., Sleep, B., Krol, M., Boparai, H. and Kocur, C., 2013. Nanoscale zero valent iron and bimetallic particles for contaminated site remediation. Advances in Water Resources, 51: 104-122.

Oostrom, M., Wietsma, T.W., Covert, M.A. and Vermeul, V.R., 2007. Zero-Valent Iron Emplacement in Permeable Porous Media Using Polymer Additions. Ground Water Monitoring & Remediation, 27(1): 122-130.

Petosa, A.R., Jaisi, D.P., Quevedo, I.R., Elimelech, M. and Tufenkji, N., 2010. Aggregation and deposition of engineered nanomaterials in aquatic environments: Role of physicochemical interactions. Environmental Science and Technology, 44(17): 6532-6549.

Quinn, J., Geiger, C., Clausen, C., Brooks, K., Coon, C., O'Hara, S., Krug, T., Major, D., Yoon, W.S., Gavaskar, A. and Holdsworth, T., 2005. Field demonstration of DNAPL dehalogenation using emulsified zero-valent iron. Environmental Science and Technology, 39(5): 1309-1318.

Rajagopalan, R. and Tien, C., 1976. Trajectory analysis of deep-bed filtration with the sphere-in-cell porous media model. Aiche Journal, 22(3): 523-533.

Saleh, N., Sirk, K., Liu, Y., Phenrat, T., Dufour, B., Matyjaszewski, K., Tilton, R.D. and Lowry, G.V., 2007. Surface modifications enhance nanoiron transport and NAPL targeting in saturated porous media. Environmental Engineering Science, 24(1): 45-57.

Sun, Y.-P., Li, X.-q., Cao, J., Zhang, W.-x. and Wang, H.P., 2006. Characterization of zero-valent iron nanoparticles. Advances in Colloid and Interface Science, 120(1-3): 47-56.

Tiraferri, A. and Sethi, R., 2009. Enhanced transport of zerovalent iron nanoparticles in saturated porous media by guar gum. Journal of Nanoparticle Research, 11(3): 635-645.

Tiraferri, A., Tosco, T. and Sethi, R., 2011. Transport and retention of microparticles in packed sand columns at low and intermediate ionic strengths: Experiments and mathematical modeling. Environmental Earth Sciences, 63(4): 847-859.

Torkzaban, S., Wan, J., Tokunaga, T.K. and Bradford, S.A., 2012. Impacts of bridging complexation on the transport of surface-modified nanoparticles in saturated sand. Journal of Contaminant Hydrology, 136-137: 86-95.

Tosco, T., Bosch, J., Meckenstock, R.U. and Sethi, R., 2012. Transport of ferrihydrite nanoparticles in saturated porous media: Role of ionic strength and flow rate. Environmental Science and Technology, 46(7): 4008-4015.

Tosco, T., Marchisio, D.L., Lince, F. and Sethi, R., 2013. Extension of the Darcy-Forchheimer Law for Shear-Thinning Fluids and Validation via Pore-Scale Flow Simulations. Transport in Porous Media, 96(1): 1-20.

Tosco, T., Petrangeli Papini, M., Cruz Viggi, C. and Sethi, R., 2014. Nanoscale iron particles for groundwater remediation: a review. Journal of Cleaner Production: DOI: 10.1016/j.jclepro.2013.12.026.

Tosco, T. and Sethi, R., 2010. Transport of non-newtonian suspensions of highly concentrated micro- and nanoscale iron particles in porous media: A modeling approach. Environmental Science and Technology, 44(23): 9062-9068.

Tufenkji, N. and Elimelech, M., 2004. Correlation equation for predicting single-collector efficiency in physicochemical filtration in saturated porous media. Environmental Science & Technology, 38(2): 529-536.

Velimirovic, M., Chen, H., Simons, Q. and Bastiaens, L., 2012. Reactivity recovery of guar gum coupled mZVI by means of enzymatic breakdown and rinsing. Journal of Contaminant Hydrology, 142-143: 1-10.

Velimirovic, M., Tosco, T., Uyttebroek, M., Luna, M., Gastone, F., De Boer, C., Klaas, N., Sapion, H., Eisenmann, H., Larsson, P.-O., Braun, J., Sethi, R. and Bastiaens, L., 2014. Field assessment of guar gum stabilized microscale zerovalent iron particles for in-situ remediation of 1,1,1-trichloroethane. Journal of Contaminant Hydrology, 164(0): 88-99.

Wexler, J.S., Trinh, P.H., Berthet, H., Quennouz, N., Du Roure, O., Huppert, H.E., Linder, A. and Stone, H.A., 2013. Bending of elastic fibres in viscous flows: The influence of confinement. Journal of Fluid Mechanics, 720: 517-544.

Xu, S.P., Gao, B. and Saiers, J.E., 2006. Straining of colloidal particles in saturated porous media. Water Resources Research, 42(12): Doi 10.1029/2006wr004948.

Xue, D. and Sethi, R., 2012. Viscoelastic gels of guar and xanthan gum mixtures provide long-term stabilization of iron micro- and nanoparticles. Journal of Nanoparticle Research, 14(11).

Yan, W., Lien, H.-L., Koel, B.E. and Zhang, W.-x., 2013. Iron nanoparticles for environmental clean-up: recent developments and future outlook. Environmental Science: Processes & Impacts, 15(1): 63-77.

Yao, K.-M., Habibian, M.T. and O'Melia, C.R., 1971. Water and waste water filtration. Concepts and applications. Environmental Science & Technology, 5(11): 1105-1112.

Zhang, W.X., 2003. Nanoscale iron particles for environmental remediation: An overview. Journal of Nanoparticle Research, 5(3-4): 323-332.

Zolla, V., Freyria, F.S., Sethi, R. and Di Molfetta, A., 2009. Hydrogeochemical and Biological Processes Affecting the Long-term Performance of an Iron-Based Permeable Reactive Barrier. J. Environ. Qual., 38(3): 897-908.

5. Appendix - Model equations in 1D and radial geometry

The model equations for transport simulations of MZVI particles dispersed in guar gum were implemented in 1D Cartesian and radial symmetry domains as summarized in this paragraph.

In all equations, it is worth to recall that in 1D Cartesian domains the Darcy velocity is a constant parameter, while in radial symmetry domains the flow velocity decreases hyperbolically with increasing distance from the origin (which corresponds in real systems to the centre of the well through which the fluid is injected):

$$q = \frac{Q}{2\pi r b} \qquad \text{(A1)}$$

A.1. Shear thinning viscosity of the MZVI slurries in dynamic conditions

The viscosity of the MZVI slurries flowing through a porous medium was modeled using the modified Cross model for shear thinning fluids, which was derived in a previous work (Gastone et al., 2014) and expresses the dependence of viscosity on the shear rate in the porous medium, $\dot{\gamma}_m$, and on the concentration of guar gum, c_{GG}:

$$\begin{cases} \mu_m(\dot{\gamma}_m, c_{GG}) = \mu_\infty(c_{GG}) + \dfrac{\mu_0(c_{GG}) - \mu_\infty(c_{GG})}{1 + [\lambda(c_{GG})\dot{\gamma}_m]^\chi} \\ \dot{\gamma}_m = \alpha \dfrac{|q|}{\sqrt{|K|\varepsilon}} \end{cases} \tag{A2}$$

where μ_0, μ_∞ λ and χ are the parameters of the Cross model, $\dot{\gamma}_m$ is the shear rate in the porous medium, K is the permeability, ε is the porosity, q is the Darcy velocity, and α is the shift factor, which is equal to 1 for the sand used in this work (see Part I).

In 1D Cartesian domains, the shear rate is influenced only by the changes in permeability and porosity, while in radial symmetry domains a further dependence on the radial distance is included through the space-dependent Darcy velocity (eq. (A1)).

The parameters of the rheological model μ_0, μ_∞ and λ were tied to the guar gum concentration c_{GG} through the relationships derived in a previous work (Gastone et al., 2014):

$$\begin{cases} \mu_0(c_{GG}) = \mu_w\left(1 + {c_{GG}}^E\right) \\ \lambda(c_{GG}) = A{c_{GG}}^B \\ \mu_\infty(c_{GG}) = \mu_{\infty,ult} - \left(\mu_{\infty,ult} - \mu_w\right)e^{-c_{GG}} \end{cases} \tag{A3}$$

where the parameters E, A, B and $\mu_{\infty,ult}$ are to be determined from fitting of experimental rheological curves. The following values were determined for guar gum solutions: E = 4.59 $A = 5.06 \cdot 10^{-4}$, $B = 4.04$, and $\mu_{\infty,ult} = 3.60 \cdot 10^{-3}$ Pa·s.

The exponent χ was conversely assumed constant, equal to 0.713.

The presence of MZVI particles dispersed in the guar gum solution does not significantly affect the viscosity of the fluid (Gastone et al., 2014), and therefore the same rheological model can be adopted for guar gum solutions with and without MZVI particles dispersed in them.

A.2. Transport of guar gum particles

The presence of guar gum undissolved residuals (solid particles and microgels) in the guar gum solutions was highlighted in a previous work (Gastone et al., 2014). In the companion paper Part I the impact of such residuals on the permeability and porosity of the porous medium was modelled in 1D Cartesian coordinates using an advection-dispersion-deposition equation implementing one irreversible interaction site for a mechanical filtration of the particles. The same interaction model can be used in radial symmetry.

A.2.1. 1D Cartesian coordinates

The transport equation developed in Part I for the transport of residual guar gum particles is

$$\begin{cases} \dfrac{\partial}{\partial t}\left(\varepsilon c_p\right)+\rho_b \dfrac{\partial s_p}{\partial t}+\dfrac{\partial}{\partial x}\left(q c_p\right)-\dfrac{\partial}{\partial x}\left(D\dfrac{\partial c_p}{\partial x}\right)=0 \\ \rho_b \dfrac{\partial s_p}{\partial t}=\varepsilon k_{ap} c_p \end{cases} \tag{A4}$$

where D is the hydrodynamic dispersion, c_P is the concentration of residual guar gum particles in the liquid phase, and s_P is the concentration of guar gum particles retained on the porous matrix due to the mechanic filtration.

The retention kinetics k_{ap} is assumed equal to

$$k_{ap} = 6.3 \cdot 10^{-3}\, s^{-1} \tag{A5}$$

which was derived in Part I from experimental results of guar gum filtration tests.

A.2.2. Radial symmetry

In radial symmetry the transport equation for guar gum residual particles becomes:

$$\begin{cases} \dfrac{\partial}{\partial t}\left(\varepsilon c_P\right) + \dfrac{\partial}{\partial t}\left(\rho_b s_P\right) + \dfrac{1}{r}\dfrac{\partial}{\partial r}\left(r q c_P\right) - \dfrac{1}{r}\dfrac{\partial}{\partial r}\left[r \varepsilon D \dfrac{\partial c_P}{\partial r} \right] = 0 \\ \rho_b \dfrac{\partial s_p}{\partial t} = \varepsilon k_{ap} c_p \end{cases} \tag{A6}$$

where the same value for the retention kinetics of eq. (A5) is adopted.

A.3. MZVI transport equations

A.3.1. 1D Cartesian coordinates

The advection-dispersion equations include two interaction sites, as discussed in Materials and Methods:

$$\begin{cases} \dfrac{\partial}{\partial t}\left(\varepsilon c_{Fe}\right)+\dfrac{\partial\left(\rho_b s_{Fe,1}\right)}{\partial t}+\dfrac{\partial\left(\rho_b s_{Fe,2}\right)}{\partial t}+\dfrac{\partial}{\partial x}\left(q c_{Fe}\right)-\dfrac{\partial}{\partial x}\left(\varepsilon D\dfrac{\partial c_{Fe}}{\partial x}\right)=0 \\ \dfrac{\partial\left(\rho_b s_{Fe,1}\right)}{\partial t}=\varepsilon k_{a,1} c_{Fe}-\rho_b k_{d,1} s_{Fe,1} \\ \dfrac{\partial\left(\rho_b s_{Fe,2}\right)}{\partial t}=\varepsilon k_{a,2}\left(1+A_2 {s_{Fe}}^{B_2}\right)c \end{cases} \quad \text{(A7)}$$

where the kinetics of deposition and release depend on flow velocity and fluid viscosity through these laws (partly derived from the literature, and partly from the experimental results discussed in this work):

$$\begin{cases} k_{a,1}\left(\mu_m, v_e\right)=C_{a,1}\dfrac{v_e}{d_{50,sand}}\eta_0\big|_{Yao}\left(\mu_m, v_e\right) \\ k_{d,1}\left(\mu_m, v_e\right)=C_{d,1}\mu_m v_e \\ k_{a,2}\left(\mu_m, v_e\right)=C_{a,2}\dfrac{v_e}{d_{50,sand}}\eta_0\big|_{Yao}\left(\mu_m, v_e\right) \end{cases} \quad \text{(A8)}$$

where $C_{a,1}$, $C_{d,1}$ and $C_{a,2}$ were determined from the results of the fitting of column tests data, and are equal respectively to where 2.01 (-), 31.35 s/kg, and $C_{a,2}$ = 0.78 (-). The shear-dependent viscosity was calculated applying the rheological model for guar gum solutions derived in a previous work (Gastone et al., 2014) (bulk rheology) and in the companion paper Part I (rheology in the porous medium).

The sedimentation rate v_s of the particles in the pore fluid is determined by the Stokes law modified for shear thinning fluids (Gastone et al., 2014):

$$v_s=\frac{1}{18}\frac{\left(\rho_{Fe}-\rho_f\right)g d_{50,Fe}^2}{\mu_m\left(\dot{\gamma}_m\right)} \quad \text{(A9)}$$

where $d_{50,Fe}$ is the average diameter of iron particles, ρ_{Fe} is the density of the iron particles, ρ_f is the density of the pore fluid (i.e. guar gum solutions), and the fluid viscosity μ_m is calculated in dynamic conditions using eq. (A2-A3).

A.3.2. Radial symmetry

The advection-dispersion equations in radial symmetry become:

$$\begin{cases} \frac{\partial}{\partial t}(\varepsilon c_{Fe}) + \frac{\partial(\rho_b s_{Fe,1})}{\partial t} + \frac{\partial(\rho_b s_{Fe,2})}{\partial t} + \frac{1}{r}\frac{\partial}{\partial r}(rqc_{Fe}) - \frac{1}{r}\frac{\partial}{\partial r}\left[r\varepsilon D_r \frac{\partial c_{Fe}}{\partial r} \right] = 0 \\ \frac{\partial(\rho_b s_{Fe,1})}{\partial t} = \varepsilon k_{a,1} c_{Fe} - \rho_b k_{d,1} s_{Fe,1} \\ \frac{\partial(\rho_b s_{Fe,2})}{\partial t} = \varepsilon k_{a,2}\left(1 + A_2 s_{Fe}{}^{B_2}\right) c \end{cases} \quad \text{(A10)}$$

where the kinetics of deposition and release are calculated from eq. (A8).

A.4. Clogging and Darcy's law

Permeability and porosity reduction due to retained guar gum particles and MZVI are modeled following a modification of the Kozeny-Carman equation:

$$\begin{cases} K = \left(\dfrac{\varepsilon}{\varepsilon_0}\right)^3 \left(\dfrac{a_0}{a}\right)^2 K_0 \\ \varepsilon = \varepsilon_0 - \dfrac{\rho_b}{\lambda_{Fe}\rho_{Fe}} s_{Fe} - \dfrac{\rho_b}{\lambda_p \rho_p} s_p \\ a = a_0 + a_{Fe}\dfrac{\rho_b}{\rho_{Fe}} s_{Fe} + a_p \dfrac{\rho_b}{\rho_p} s \end{cases} \tag{A11}$$

The Darcy's law modified for shear thinning fluids was adopted for the calculation of pressure gradients:

$$-\nabla p = \frac{\mu_m(\dot{\gamma}_m)}{K} q \tag{A12}$$

where the permeability is given by eq. (A11), and the fluid viscosity in dynamic conditions is given by eq. (A2-A3).

Figures

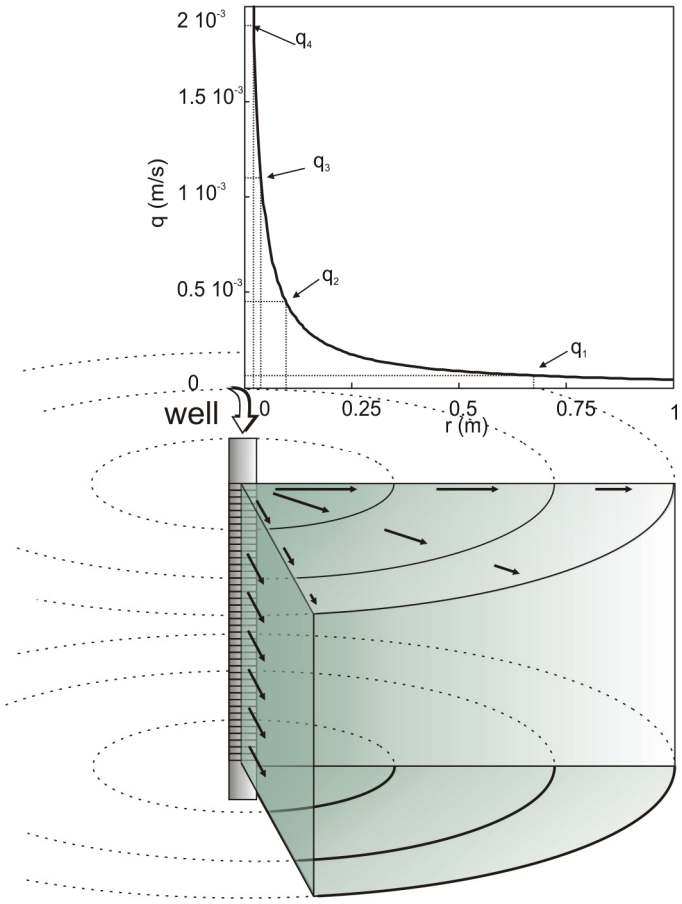

Figure 1: Radial domain for MZVI injection through a well, and hyperbolic decrease of Darcy velocity with increasing radial distance. The Darcy velocities selected for 1D column transport tests, corresponding to different distances from the injection well, are also reported.

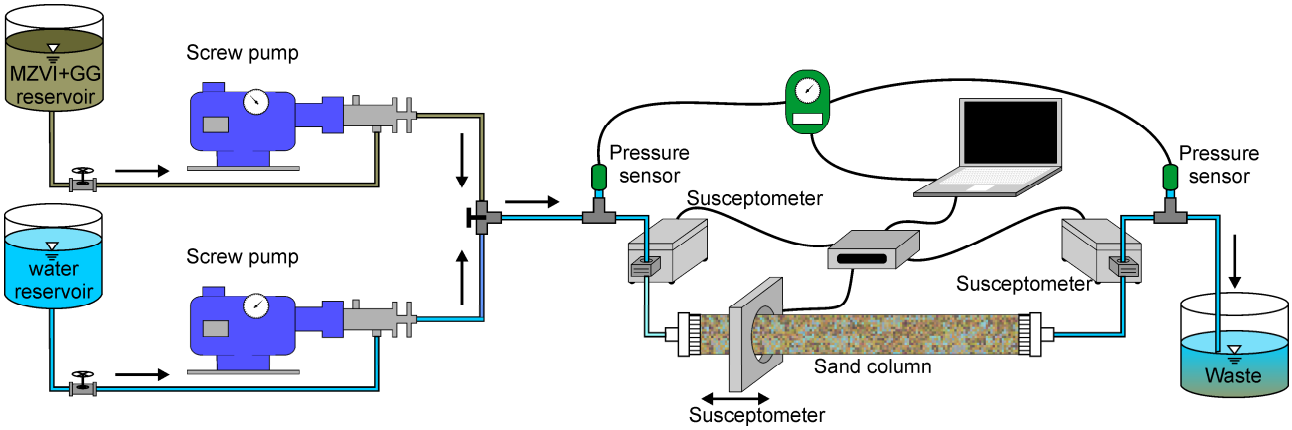

Figure 2: Experimental setup for iron transport tests.

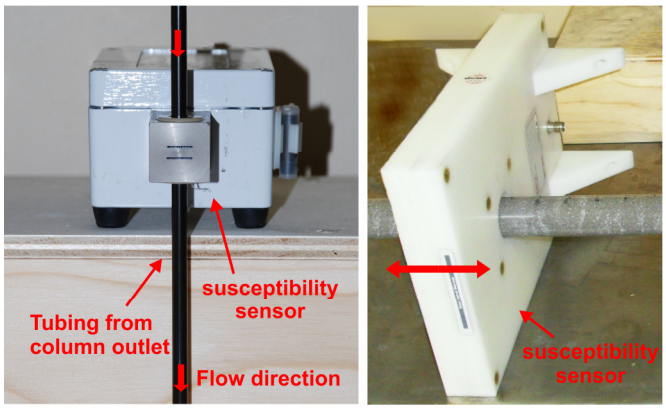

(a) (b)

Figure 3: Susceptibility sensors (Bartington, UK) (a) connected to the column outlet for in-line magnetic susceptibility measurements (MS2G), and (b) positioned along the column for profile measurements (MS2C).

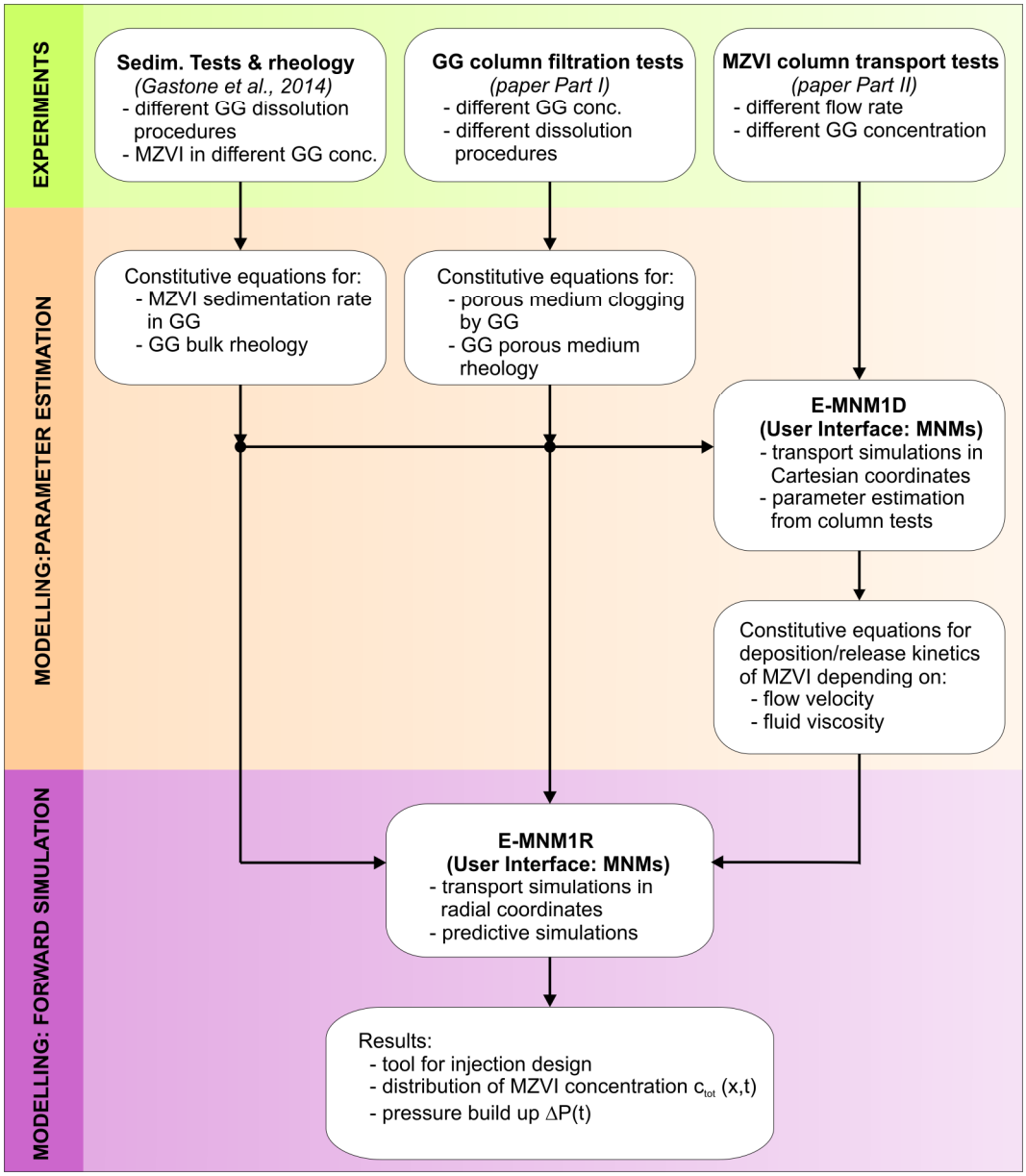

Figure 4: Procedure for the dimensioning of a permeation injection of MZVI slurries: from lab experiments to the modeling tools. The software E-MNM1D, E-MNM1R, and the user interface MNMs can be downloaded at www.polito.it/groundwater/software.

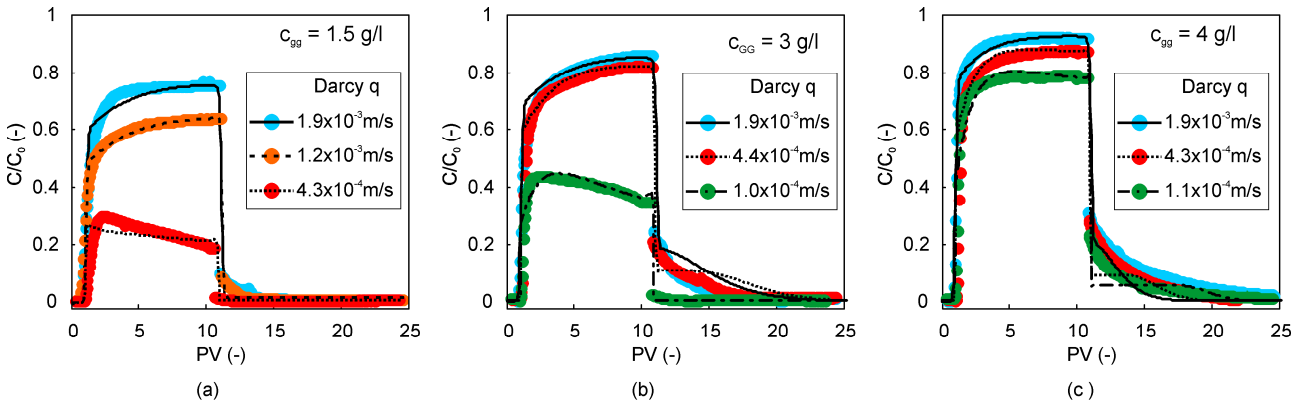

Figure 5: Breakthrough curves of column transport tests reported as normalized concentration C/C_0 as a function of the number of pore volumes injected, for MZVI particles (20 g/l) dispersed in solutions of guar gum at 1.5 g/l (a), 3 g(l) and 4 g(l), for several velocities. Experimental data (point values) and modeled curves (black lines) are reported.

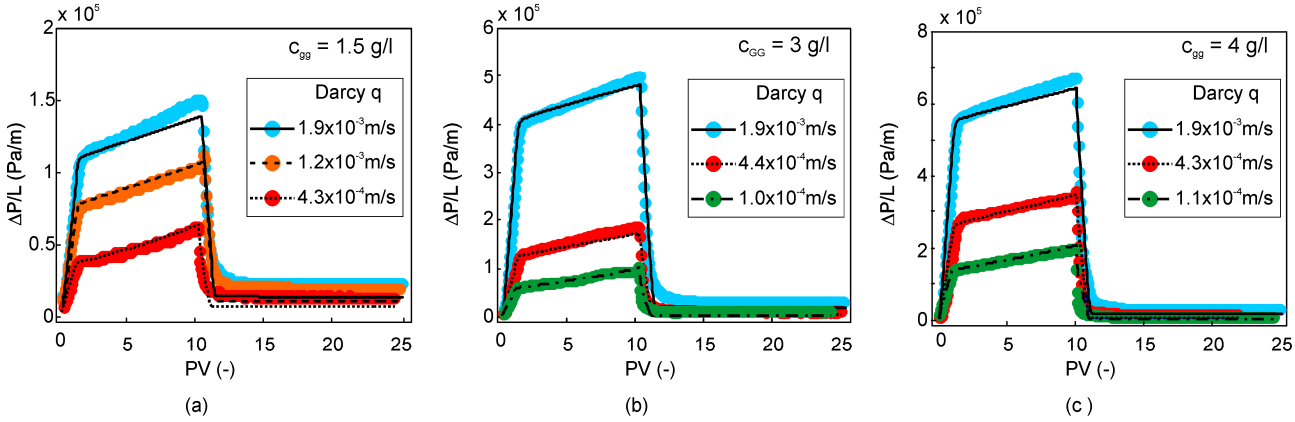

Figure 6: Normalized pressure drop $\Delta P/L$ during column transport tests reported as a function of the number of pore volumes injected, for MZVI particles (20 g/l) dispersed in solutions of guar gum at 1.5 g/l (a), 3 g(l) and 4 g(l), for several flow velocities. Experimental data (point values) and modeled curves (black lines) are reported.

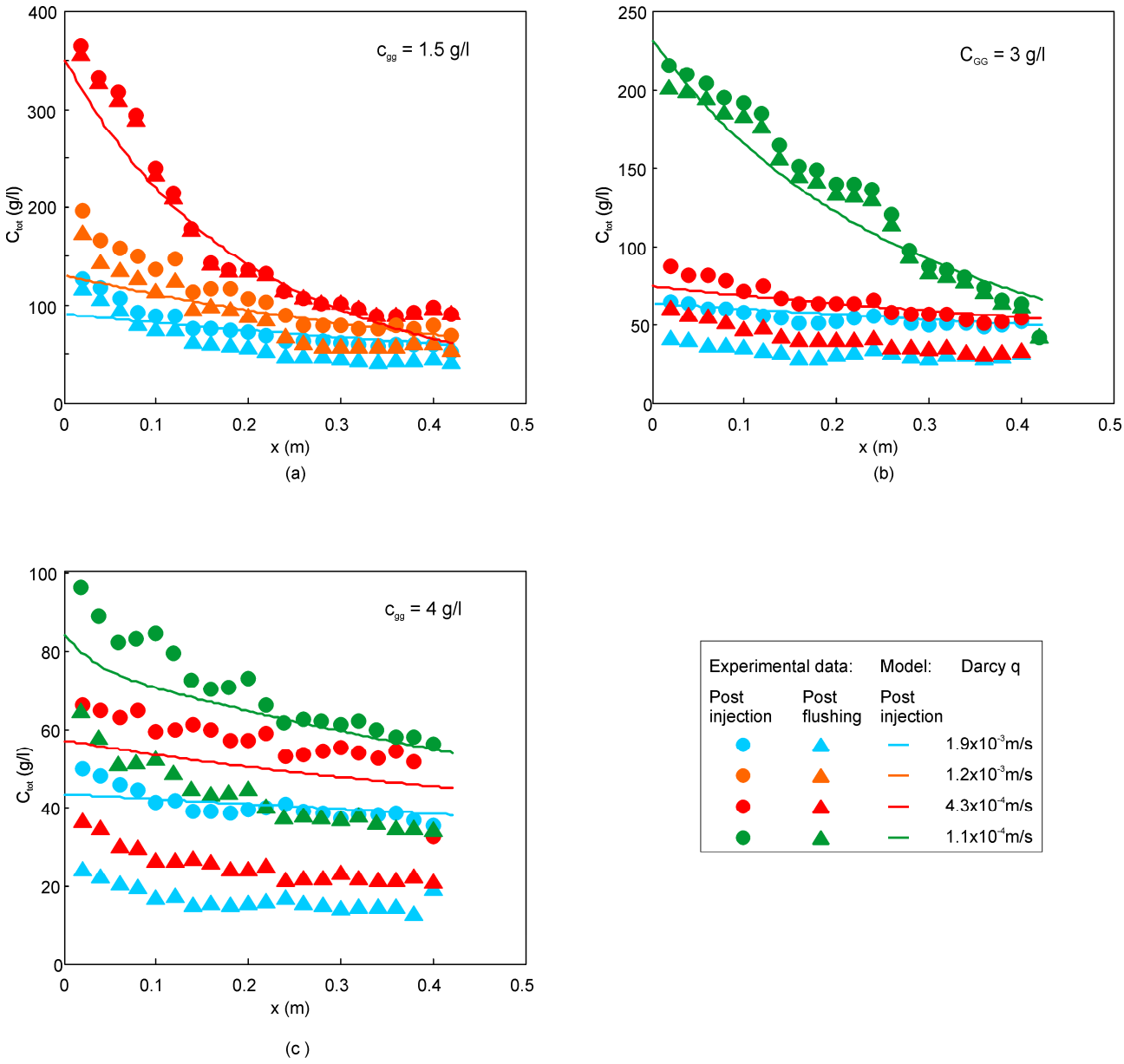

Figure 7: Profiles of total iron concentration C_{tot} along the columns measured in MZVI transport tests, for particles (20 g/l) dispersed in solutions of guar gum at 1.5 g/l (a), 3 g(l) and 4 g(l), for several flow velocities. The experimental profiles are measured after the iron injection, before (circles) and after (triangles) flushing. The model profiles (color lines) are calculated before flushing.

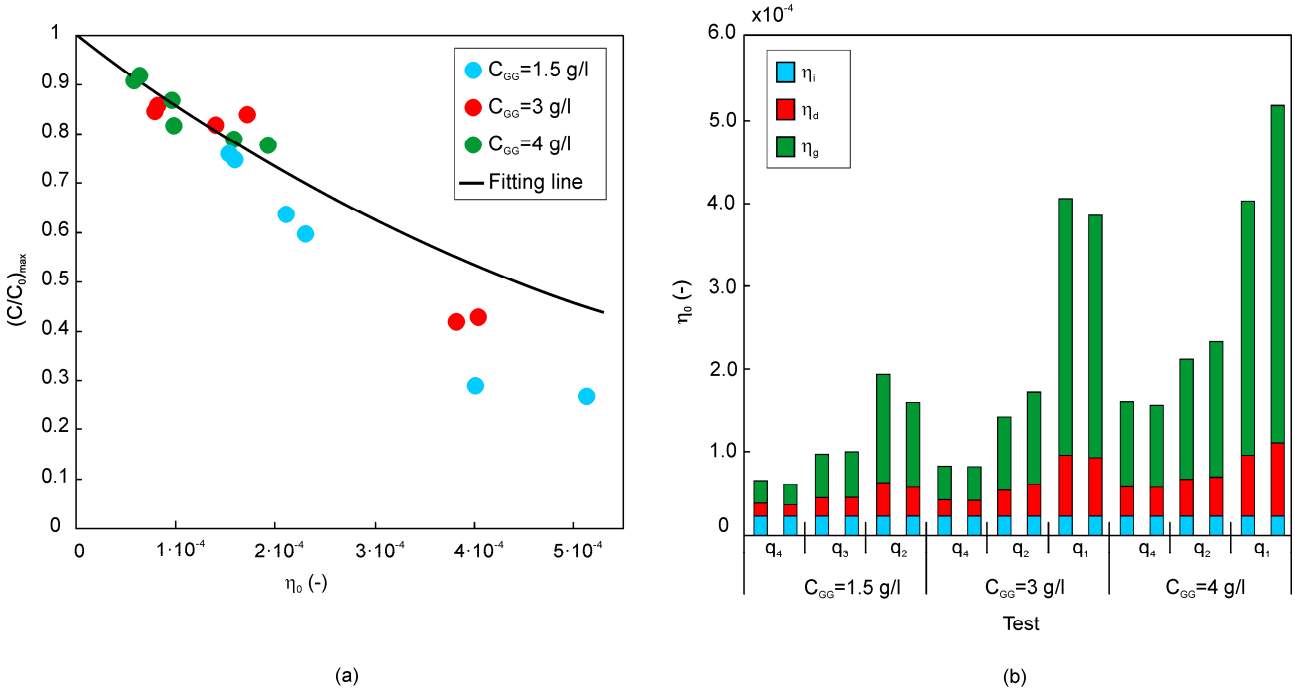

(a) (b)

Figure 8: Steady state breakthrough concentration $(C/C_0)_{max}$ as a function of the removal efficiency η_0 with model eq. (12) (a), and removal efficiencies due to interception (η_I), diffusion (η_D) and gravitational settling (η_G) for each test (b).

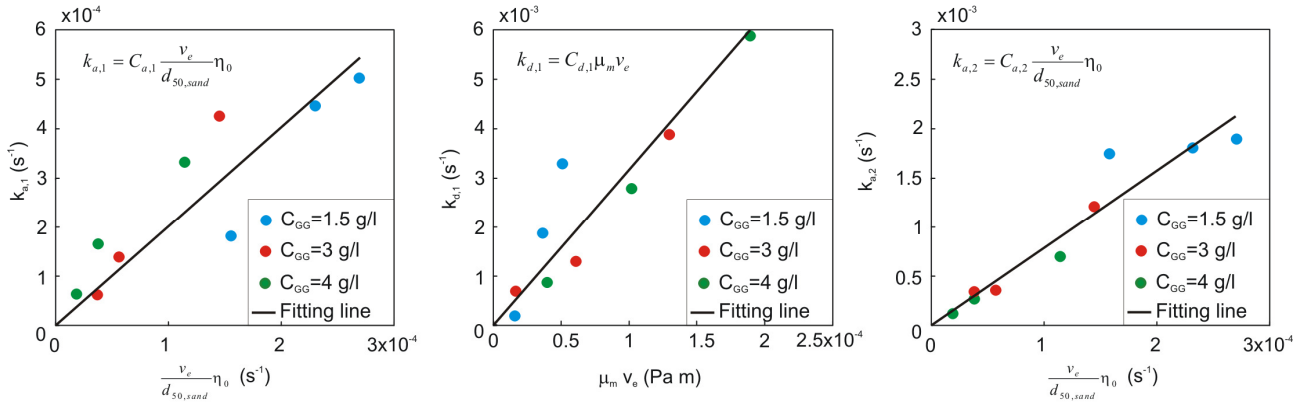

(a) (b) (c)

Figure 9: Attachment coefficient $k_{a,1}$ of site 1 as a function of the the group $v_e/d_{50,sand}\cdot\eta_0$ (a), detachment coefficient $k_{d,1}$ of site 1 as a function of $\mu_m\ v_e$ (b) and attachment rate $k_{a,2}$ of site 2 as a function of the group the group $v_e/d_{50,sand}\cdot\eta_0$ (c).

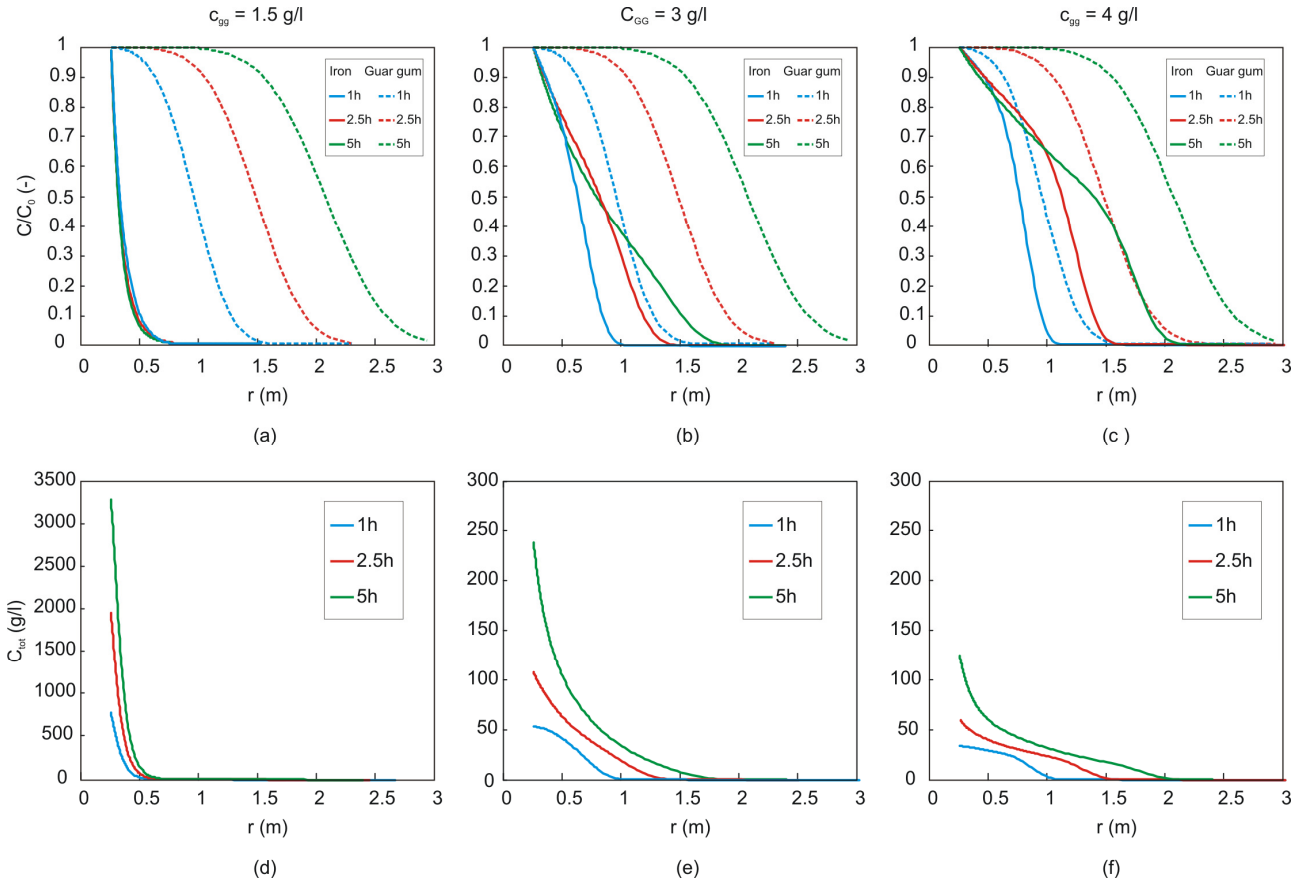

Figure 10: Simulation of radial injection of 20 g/l of iron particles at a discharge rate of 1 m^3/h per unit length of the well screen: profiles of suspended iron concentration normalized to the injected one (C/C_0) as a function of radial distance from the injection point (a-c) and corresponding profiles of total (suspended + retained) iron concentration C_{tot} for iron particles (d-f) dispersed in 1.5 g/l (a,d), 3 g/l (b,e), 4 g/l (c,f) of guar gum. The profiles are calculated after 1h, 2.5h, and 5 h of injection.

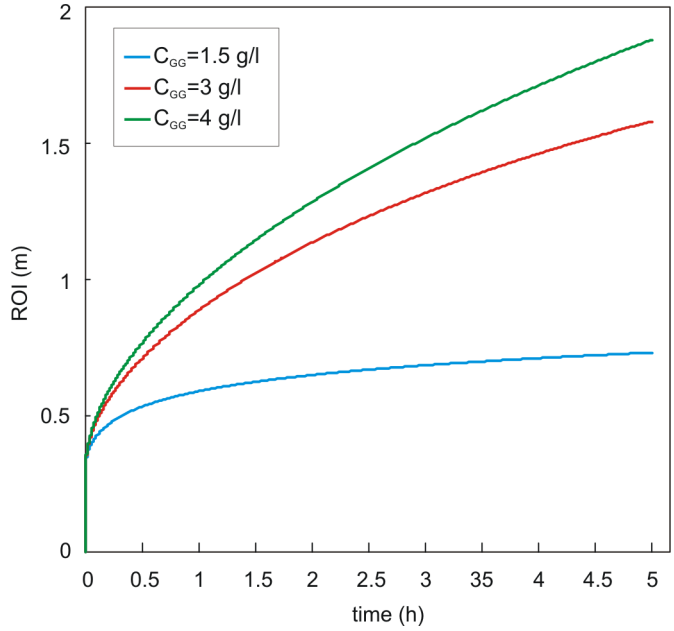

Figure 11: Radius of influence ROI for a target concentration of 5 g/l as a function of time.

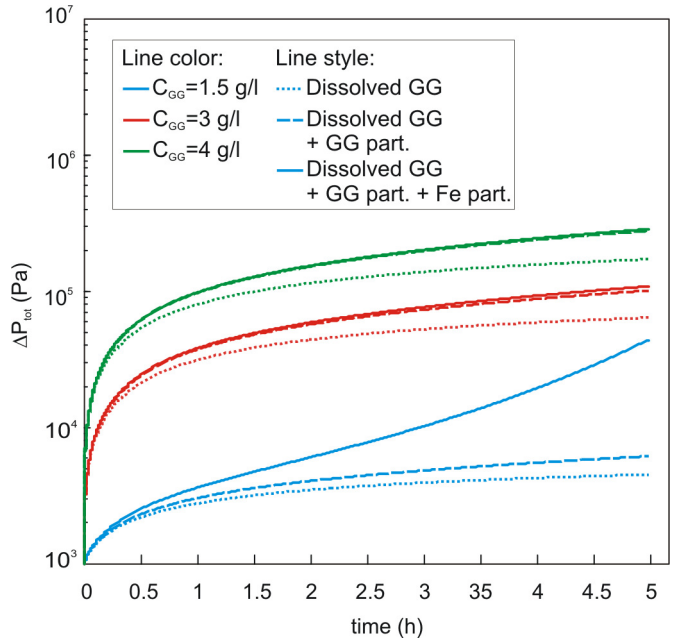

Figure 12: Total pressure build up as a function of time (a) for the injection of 20 g/l of iron particles dispersed in 1.5, 3 and 4 g/l of guar gum at a discharge rate of 1 m^3/h (solid lines). For

comparison, pressure build obtained injecting guar gum without undissolved guar gum particles (dotted lines) and with undissolved guar gum particles but without iron (dashed lines).

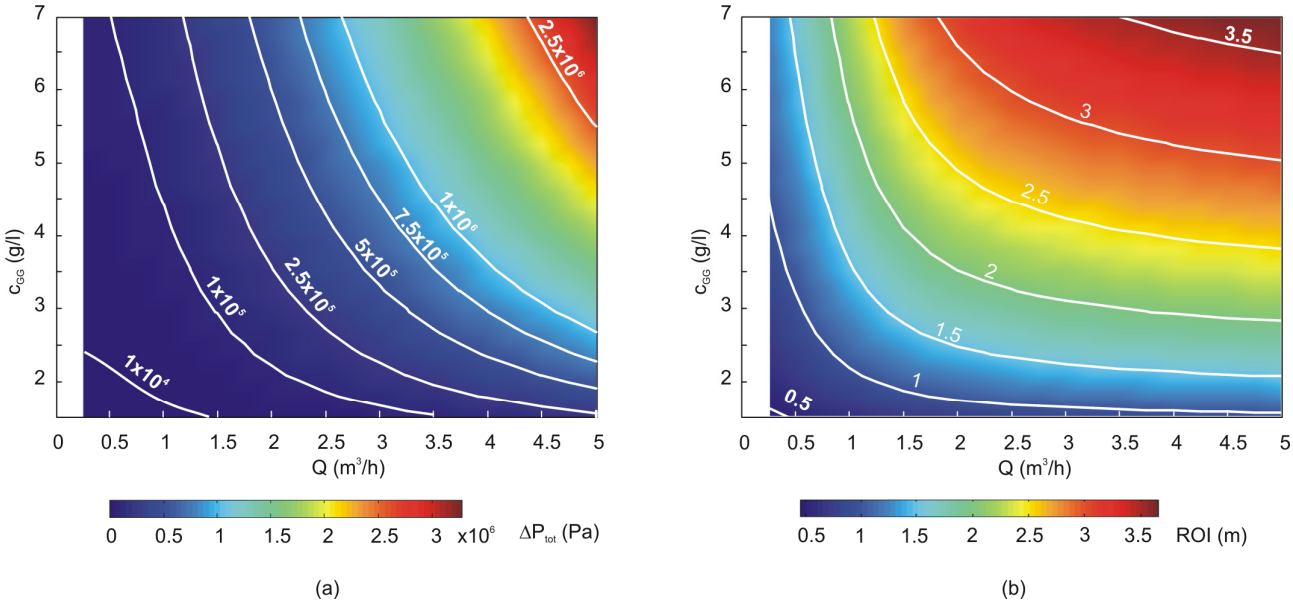

Figure 13: Map of pressure build up ΔP_{tot} (a) and radius of influence ROI for a target concentration of 5 g/l (b) for the injection of 5 m^3 of MZVI slurry with iron concentration of 20 g/l. On the axes the variable guar gum concentration c_{GG} and discharge rate Q are reported.

Tables

Table 1: Darcy velocity q, transit time of 1 pore volume t_{PV} and steady state outlet concentration $(C/C_0)_{ss}$; mass balances after injection and flushing; slurry viscosity in dynamic conditions (calculated using equation A2-A3) and corresponding sedimentation rate of the particles in the pores v_s; comparison between sedimentation time in the pores, t_s (calculated considering as sedimentation path half the pore diameter d_{50}), and breakthrough time t_{PV}.

Guar gum conc. c_{GG} (g/l)	Flow rate q (m/s)		Time of 1 PV t_{PV} (s)	Steady state outlet conc. $(C/C_0)_{max}$ (-)	Mass balance M_{OUT}/M_{INj} After inj.	Mass balance M_{OUT}/M_{INj} After flush.	Shear rate $\dot{\gamma}_m$ (s^{-1})	Dynamic viscosity μ_m (Pa s)	Sed. rate v_s (m/s)	Sed. time in pores t_s (s)	t_s/t_{PV}
1.5	q_4	$1.85 \cdot 10^{-3}$	84.7	0.75	59.8%	66.3%	227.5	$1.03 \cdot 10^{-2}$	$1.74 \cdot 10^{-6}$	89.2	1.05
		$1.86 \cdot 10^{-3}$	84.4	0.76	57.8%	63.5%	228.9	$1.07 \cdot 10^{-2}$	$1.74 \cdot 10^{-6}$	86.1	1.02
	q_3	$1.21 \cdot 10^{-3}$	129.6	0.64	46.2%	52.2%	148.1	$1.12 \cdot 10^{-2}$	$1.60 \cdot 10^{-6}$	62.1	0.48
		$1.18 \cdot 10^{-3}$	132.9	0.60	44.8%	48.8%	144.6	$1.02 \cdot 10^{-2}$	$1.75 \cdot 10^{-6}$	85.5	0.64
	q_2	$4.32 \cdot 10^{-4}$	363.4	0.29	18.9%	19.7%	63.4	$1.48 \cdot 10^{-2}$	$1.21 \cdot 10^{-6}$	93.4	0.26
		$4.34 \cdot 10^{-4}$	362.6	0.27	17.8%	19.9%	53.0	$1.12 \cdot 10^{-2}$	$1.60 \cdot 10^{-6}$	93.7	0.27
3	q_4	$1.92 \cdot 10^{-3}$	81.7	0.86	65.8%	78.4%	285.7	$2.51 \cdot 10^{-2}$	$7.17 \cdot 10^{-7}$	210.2	2.57
		$1.94 \cdot 10^{-3}$	80.9	0.85	62.9%	74.0%	289.4	$2.55 \cdot 10^{-2}$	$7.04 \cdot 10^{-7}$	213.0	2.63
	q_3	$4.41 \cdot 10^{-4}$	356.1	0.82	58.8%	70.1%	52.5	$5.13 \cdot 10^{-2}$	$3.50 \cdot 10^{-7}$	325.8	0.91
		$4.46 \cdot 10^{-4}$	352.8	0.84	55.2%	65.0%	53.2	$3.94 \cdot 10^{-2}$	$4.55 \cdot 10^{-7}$	329.3	0.93
	q_1	$1.02 \cdot 10^{-4}$	1534.8	0.43	33.8%	34.2%	15.6	$6.21 \cdot 10^{-2}$	$2.89 \cdot 10^{-7}$	545.4	0.36
		$1.03 \cdot 10^{-4}$	1527.4	0.42	32.7%	33.0%	15.7	$6.56 \cdot 10^{-2}$	$2.73 \cdot 10^{-7}$	549.0	0.35
4	q_4	$1.92 \cdot 10^{-3}$	81.9	0.92	75.9%	95.4%	274.2	$3.68 \cdot 10^{-2}$	$4.87 \cdot 10^{-7}$	335.5	4.10
		$1.94 \cdot 10^{-3}$	80.9	0.91	68.7%	90.1%	278.0	$4.07 \cdot 10^{-2}$	$4.40 \cdot 10^{-7}$	340.6	4.21
	q_3	$4.27 \cdot 10^{-4}$	367.5	0.87	69.2%	83.9%	59.4	$8.84 \cdot 10^{-2}$	$2.03 \cdot 10^{-7}$	693.9	1.89
		$4.33 \cdot 10^{-4}$	363.5	0.82	64.3%	83.3%	60.1	$8.40 \cdot 10^{-2}$	$2.13 \cdot 10^{-7}$	702.7	1.93
	q_1	$1.08 \cdot 10^{-4}$	1450.5	0.78	63.7%	73.8%	16.5	$1.40 \cdot 10^{-1}$	$1.28 \cdot 10^{-7}$	1508.7	1.04
		$1.07 \cdot 10^{-4}$	1462.9	0.79	59.0%	70.1%	16.4	$1.80 \cdot 10^{-1}$	$9.94 \cdot 10^{-8}$	1508.7	1.03

Table 2: Model parameters from fitting of the column tests experimental data.

	Parameter	1.5 g/l			3 g/l			4 g/l		
		q_{MAX}	$q_{0.5MAX}$	q_{MEAN}	q_{MAX}	q_{MEAN}	q_{MIN}	q_{MAX}	q_{MEAN}	q_{MIN}
Site 1	$k_{a,1}$ [s^{-1}]	$5.0 \cdot 10^{-3}$	$4.5 \cdot 10^{-3}$	$1.9 \cdot 10^{-3}$	$4.3 \cdot 10^{-3}$	$1.4 \cdot 10^{-3}$	$6.5 \cdot 10^{-4}$	$3.3 \cdot 10^{-3}$	$1.7 \cdot 10^{-3}$	$6.5 \cdot 10^{-4}$
	$k_{d,1}$ [Pa m]	$3.3 \cdot 10^{-3}$	$1.9 \cdot 10^{-3}$	$2.0 \cdot 10^{-4}$	$3.9 \cdot 10^{-3}$	$1.3 \cdot 10^{-3}$	$7.0 \cdot 10^{-4}$	$6.0 \cdot 10^{-3}$	$2.8 \cdot 10^{-3}$	$9.0 \cdot 10^{-4}$
Site 2	$k_{a,2}$ [s^{-1}]	$1.9 \cdot 10^{-3}$	$1.8 \cdot 10^{-3}$	$1.7 \cdot 10^{-3}$	$1.2 \cdot 10^{-3}$	$3.5 \cdot 10^{-4}$	$3.4 \cdot 10^{-4}$	$6.9 \cdot 10^{-4}$	$2.6 \cdot 10^{-4}$	$1.1 \cdot 10^{-4}$
	A_2 [-]	11.0								
	B_2 [-]	0.61								
Clogging parameters	a_{Fe} [L^{-1}]	$4.56 \cdot 10^{5}$								
	λ_{Fe} [-]	0.45								